Accepted Manuscript

Geochemical signature and reservoir conditions of Early Jurassic calc-alkaline volcanic rocks from Lonco Trapial Formation, Central Patagonia

Claudia Zaffarana, Gloria Gallastegui, Silvia Lagorio, Stella Poma, Alicia Busteros, Samanta Serra Varela, Darío Orts, Diego Silva Nieto, Raúl Giacosa, Víctor Ruiz González, Carla Puigdomenech, Bárbara Boltshauser, Rubén Somoza

PII: S0895-9811(18)30184-6

DOI: 10.1016/j.jsames.2018.09.006

Reference: SAMES 2003

To appear in: *Journal of South American Earth Sciences*

Received Date: 24 May 2018

Revised Date: 22 August 2018

Accepted Date: 18 September 2018

Please cite this article as: Zaffarana, C., Gallastegui, G., Lagorio, S., Poma, S., Busteros, A., Varela, S.S., Orts, Darí., Silva Nieto, D., Giacosa, Raú., Ruiz González, Ví., Puigdomenech, C., Boltshauser, Bá., Somoza, Rubé., Geochemical signature and reservoir conditions of Early Jurassic calc-alkaline volcanic rocks from Lonco Trapial Formation, Central Patagonia, *Journal of South American Earth Sciences* (2018), doi: https://doi.org/10.1016/j.jsames.2018.09.006.

Geochemical signature and reservoir conditions of Early Jurassic calc-alkaline volcanic rocks from Lonco Trapial Formation, Central Patagonia

Claudia Zaffarana[1,2,*], Gloria Gallastegui[3], Silvia Lagorio[4], Stella Poma[2,5], Alicia Busteros[4], Samanta Serra Varela[1,2], Darío Orts[1,2], Diego Silva Nieto[4], Raúl Giacosa[1,4], Víctor Ruiz González[2,5], Carla Puigdomenech[2,5] , Bárbara Boltshauser[1,2] and Rubén Somoza[2]

[1] Universidad Nacional de Río Negro, Av. Julio A. Roca 1242 General Roca (8332), Pcia. de Río Negro, Argentina. * czaffarana@unrn.edu.ar

[2] Consejo Nacional de Investigaciones Científicas y Técnicas (CONICET)

[3] Instituto Geológico y Minero de España (IGME)

[4] Servicio Geológico Minero Argentino (SEGEMAR)

[5] Departamento de Geología de la FCEyN de la Universidad de Buenos Aires, Argentina

Abstract

Central Patagonia is traversed by a belt of Early to Middle Jurassic calc-alkaline intermediate volcanic rocks interspersed with more felsic volcanic rocks which are associated with the widespread magmatism that took place during Gondwana break-up times. This work uses K-Ar and Ar-Ar dating and whole-rock and phenocryst (plagioclase, amphibole, clinopyroxene and titanomagnetite) compositional data to refine the age, geochemical signature and reservoir conditions of these volcanic rocks, which are known as Lonco Trapial Formation. The andesites, dacites and trachydacites which were the object of this study have either amphibole or clinopyroxene as the main

mafic phenocryst (amphibole-bearing and clinopyroxene-bearing volcanic rocks, respectively), though amphibole is the main mafic phase. Despite the calc-alkaline signature a mild alkaline affinity emerges from some whole-rock trace elements content and from mineral chemistry (amphibole, clinopyroxene and titanomagnetite compositions). The magmatic evolution of the Lonco Trapial andesites, dacites and trachydacites was governed by fractionation of amphibole, clinopyroxene, plagioclase, titanite, titanomagnetite and apatite. Amphibole phenocrysts show an overall normal chemical zoning. The cores of the amphiboles crystallized over a temperature range of 869 to 916 °C, whereas the rims crystallized over a tempeture range of 826 to 867 °C. Shallow to intermediate depths (2-8 kbar, ~7-26 km) were inferred from geobarometric calculations. Crystallization temperatures are slightly higher in the clinopyroxene-bearing volcanic rocks, consistent with their more primitive character. The geobarometric estimations of this work are coherent with the lack of marine ingressions and with geophysical estimations which suggest that the Early Jurassic Moho depth would have been ≤35 km. The combination of whole-rock and mineral geochemistry is consistent with an extensional affinity for this paleo-volcanic belt.

Keywords: andesite; Jurassic; mineral chemistry; whole-rock geochemistry; Central Patagonia

1. INTRODUCTION

Early Jurassic times in Patagonia were characterized by widespread magmatism linked to the early stages of Gondwana break-up. This magmatism is known as the Chon Aike Volcanic Province, one of the largest rhyolitic provinces in the world which also extends to the Antarctic Peninsula (Pankhurst et al., 1998; 2000; Riley et al., 2001). The age of this magmatism becomes younger southwards, preceding the opening of the South Atlantic Ocean in the Early Cretaceous (Pankhurst et al., 2000). This volcanism

starts in northeastern Patagonia in the Early Jurassic, with the V1 volcanic event (188-178 Ma), and is coeval with the peak of the Karroo-Ferrar basaltic volcanism. It was then followed in southern Patagonia and northern Antarctic Peninsula by the Middle Jurassic volcanic event V2 (172-162 Ma), and by the Late Jurassic volcanic event V3 (157-153 Ma) which migrated to the Andes Cordillera (Féraud et al., 1999; Pankhurst et al., 2000 and references therein).

Central Patagonia is traversed by a N-S belt of calc-alkaline intermediate volcanic rocks interspersed with more felsic volcanics and with sedimentary rocks known as the Lonco Trapial Formation (Page and Page, 1993). The Lonco Trapial lavas were considered the more mafic counterparts of the predominantly rhyolitic Chon Aike Volcanic Province and part of the V1 volcanic event (Gust et al., 1985; Pankhurst et al., 1998; 2000; Franzese et al., 2002; Zaffarana and Somoza, 2012; Benedini and Gregori, 2013; Cúneo et al., 2013; Bouhier et al., 2017). This volcanism was in a back-arc position with respect to the activity of a western short-lived Early Jurassic magmatic arc known as the Subcordilleran Plutonic Belt (Fig. 1a; Gordon and Ort, 1993; Haller et al., 1999; Rapela et al., 2005).

This work aims to refine the origins of the Lonco Trapial Formation volcanic rocks using new measurements of mineral and whole-rock major and trace element compositions (e.g. Sas et al., 2017). The sample suite comprises mainly Early Jurassic andesites, dacites and trachydacites from the locality of Gastre (Fig. 1b). Our data are used to constrain magma type, petrogenetic processes, magma storage conditions (temperature, pressure, fO_2) and parental melt compositions. Our analysis recovers an extensional signature from these predominantly calc-alkaline magmas.

2. GEOLOGICAL SETTING

2.1. Early Jurassic igneous and sedimentary units in the North Patagonian

74 **Massif**

75 The distribution of Early Jurassic rocks in Patagonia between 40º and 44º S is shown in
76 Fig. 1a. The Early Jurassic units of the North Patagonian Massif can be divided into
77 three domains: eastern, central and western (Fig. 1a). Within the eastern domain, the
78 Early Jurassic rocks are predominantly magmatic, comprised of the rhyolitic volcanic
79 rocks of the Marifil Formation (Pankhurst et al., 1993; Pankhurst and Rapela, 1995;
80 Féraud et al., 1999) and by their intrusive counterparts known as the El Sótano
81 Granodiorite (Sato et al., 2004) and as the Flores Granite (Pankhurst et al., 1993).

82 In the central domain, the Early Jurassic rocks are predominantly volcanic and andesitic
83 (Fig. 1a). Following Page and Page (1993), the Lonco Trapial Formation is used here to
84 refer to the volcanic belt of predominantly intermediate composition of Central
85 Patagonia. North of Gastre, the Lonco Trapial Formation intermediate volcanics
86 interdigitate with the Early Jurassic felsic volcanics of Garamilla Formation (Nullo,
87 1978; Franzese et al., 2002; Benedini and Gregori, 2013). South of Gastre (near Paso
88 del Sapo and further south), the Lonco Trapial Formation forms part of the early infill
89 of the Cañadón Asfalto basin (Figari and Courtade, 1993; Cortiñas, 1996; Cúneo et al.,
90 2013; Figari et al., 2015; Hauser et al., 2017; Bouhier et al. 2017), overlying the syn-rift
91 deposits of Las Leoneras Formation (Cúneo et al., 2013; Fig. 1a).

92 The NNW-SSE Early Jurassic Pampa de Agnia basin extends to the western (and partly
93 central) domain of the North Patagonian Massif (Fig. 1a, Vizán, 1998; Suárez and
94 Márquez, 2007). The sedimentary rocks of the Pampa de Agnia basin are intruded by
95 the Early Jurassic mafic-ultramafic suite of the Tecka and Cresta de los Bosques
96 formations (Page, 1984; Poma, 1986; Féraud et al., 1999; Page and Page, 1999). The
97 gabbros and sedimentary rocks are intruded by the Subcordilleran Plutonic Belt, a
98 NNW-SSE trending batholith of Early Jurassic age (Fig. 1a; Gordon and Ort, 1993;

Haller et al., 1999; Rapela et al. 2005). Lonco Trapial Formation lavas are in a back-arc position with respect to the activity of the Early Jurassic magmatic arc represented by the Subcordilleran Plutonic Belt (Fig. 1a).

2.2. Local geology and sampling: the Lonco Trapial Formation in Gastre

This work is focused on volcanic rocks from the Lonco Trapial Formation in Gastre (Fig. 1a). Here, the oldest rocks are Late Paleozoic metamorphic rocks of the Calcatapul (Proserpio, 1978) and Cushamen formations (Volkheimer, 1964; López de Luchi and Cerredo, 2008). Two later magmatic suites include: the Late Paleozoic granites of the Gondwanic cycle and the Late Triassic granites of the Central Patagonian Batholith (Rapela et al., 1991; Rapela and Pankhurst, 1992; Pankhurst et al., 2006; López de Luchi and Cerredo, 2008; Zaffarana et al., 2017). The Jurassic volcano-sedimentary Lonco Trapial Formation (Taquetrén Formation of Nullo and Proserpio, 1975; Proserpio, 1978) rests on a highly irregular paleosurface carved into these granitoids.

The Lonco Trapial Formation in Gastre hosts a volumetrically important eruptive suite associated with thick volcaniclastic conglomerates. The volcanic facies are mainly represented by andesitic lavas and breccias, while the subvolcanic facies consist of many porphyries and dikes of the same composition. There are also subordinate pyroclastic facies composed of tuffaceous beds mainly corresponding to dacitic ignimbrites. Representative samples collected in this study correspond to lava flows (T1, T0, JZ6-4 and G3-157), dikes (G3-134) and porphyries (G2-63). A summary of the ages, locations and studies that were performed is presented in Table 1, and locations are shown in Fig. 1.

3. ANALYTICAL TECHNIQUES

123 Whole-rock major and trace elements were determined using ICP, ICP-MS and ICP-
124 AES at Activation Laboratories, Ontario, Canada (ACTLABs) and at the SGS
125 laboratory (Peru). Results are presented in Table 1-Appendix.

126 Sample G2-63 was dated by ^{40}Ar-^{39}Ar in amphibole at the Geochronological Laboratory
127 of SERNAGEOMIN (Chile) and sample G3-134 was dated by whole-rock K-Ar at
128 Actlabs (Ontario, Canada). In the former, the system is equipped with two extraction
129 lines of radiogenic Ar gas, which are aligned with a Stanelco induction furnace, with a
130 maximum power of 7.5 kW. The extracted Ar is purified through two extraction lines of
131 Ar and is analyzed in a semi-automatic mass spectromet er where the total content of
132 ^{40}Ar in the sample is detected (radiogenic ^{40}Ar and ^{40}Ar atmospheric). The measurement
133 of K in the sample is analyzed in an equivalent aliquot, through X-ray fluorescence in
134 the Chemical Laboratory of SERNAGEOMIN.

135 Mineral phases were analyzed by WDS at the Technical-Scientific Services of Oviedo
136 University (Spain) using a Cameca SX-100 electron microprobe with a voltage intensity
137 of 15 kv, current of 15 nA, and acquisition time of 10 s per element. A combination of
138 silicates and oxides was used for calibration. Results are presented in Table 2-
139 Appendix.

140 ICP-MS laser ablation measurements of amphibole separates were done at the GZG,
141 University of Göttingen (Germany) on a Perkin Elmer DRC II equipped with a Lambda
142 Physics Compex 110 Ar-F Laser at 193 nm, using a Geol-Las optical bank. Ar carrier
143 gas was used and a low-volume custom-made sample chamber. Individual elements
144 were measured after 10 milliseconds dwell time with an integration time for the
145 measured signal of 60 seconds (on average). The estimated major element composition
146 (Si) of the respective mineral was used as internal standard. Results are presented in
147 Table 3-Appendix.

148 EDS data of amphibole crystals were obtained in the Centro de Microscopías
149 Avanzadas (CMA), Facultad de Ciencias Exactas y Naturales, Universidad de Buenos
150 Aires (FCEN-UBA). The equipment is characterized by an Energy Dispersive X-Ray
151 Microanalysis hardware (EDS), Inca Energy, Oxford Instruments, coupled with a SEM
152 Zeiss Supra 40 scanning electron microscope equipped with a field emission gun. The
153 images were taken with in-lens detector and 5 kV acceleration voltage. The applied
154 standards were $CaCO_3$ for C, SiO_2 for O and Si, Al_2O_3 for Al, wollastonite for Ca,
155 MgF_2 for F and MgO for Mg. Results are presented in Table 4-Appendix.

156 **4. K-AR AND AR-AR DATING**

157 The age of Lonco Trapial Formation is constrained between Early and Middle Jurassic
158 time (Page and Page, 1993; Bouhier et al., 2017). In this work we dated some samples
159 that confirmed an Early Jurassic age within the V1 volcanic event (Pankhurst et al.,
160 2000). This period was characterized by ongoing magmatism to the west
161 (Subcordilleran Plutonic Belt, Fig. 1).
162 Sample G2-63 presented a good ^{40}Ar-^{39}Ar plateau age for amphibole of 178.9 ± 1.1 Ma
163 (94.1 % of ^{39}Ar released on 5 of the 9 steps, MSWD=0.49; Fig. 2a, Table 1). The
164 integrated age is 175.9 ± 1.4 Ma, and the isochron age is 178.7 ± 1.8 Ma (MSWD=0.63,
165 with 5 out of 9 steps). The steps disregarded in the isochron and plateau ages are the
166 low temperature ones, representing only 4.9 % of the total ^{39}Ar released. The $^{40}Ar/^{36}Ar$
167 intercept is a bit higher than the atmospheric ratio (300 ± 40, Fig. 2b), suggesting that
168 some excess argon is present in the amphiboles, however, the three ages broadly
169 coincide. The accepted age for this sample is the plateau age.
170 The andesitic dike represented by sample G3-134 yielded a K-Ar whole-rock age of
171 191.6 ± 5.2 Ma (% K=1.88, ^{40}Ar radiogenic= 14.492 ml/g, % ^{40}Ar air= 37.6). Sample
172 T0 yielded an ^{40}Ar-^{39}Ar age in amphibole of 185.39 ± 0.99 Ma, whereas sample T1

presented two overlapping ^{40}Ar-^{39}Ar ages for amphibole of 184 ± 5 Ma and of 182.8 ± 1.3 Ma (Zaffarana and Somoza, 2012). The reported ages are consistent with the paleomagnetic pole location, as the paleomagnetic vector isolated in sample JZ6-4 is consistent with the Early Jurassic mean direction in the area of study. This sample was part of the data set used to define an Early Jurassic paleomagnetic pole by Zaffarana and Somoza (2012) (Table 1). The clinopyroxene-bearing sample G3-157 was intercalated within the amphibole-bearing volcanic rocks typical of Lonco Trapial Formation in Gastre, therefore a Lower Jurassic age is expected for this sample.

5. CLASSIFICATION AND PETROGRAPHY

The volcanic rocks of Lonco Trapial Formation have porphyritic (~50 modal % phenocrysts) to glomeroporphyritic textures (Fig.3). They have been classified as andesite, dacites and trachydacites in the major element classification diagram (TAS, Fig. 4a). Andesitic lavas and dikes have either amphibole (amphibole-bearing volcanic rocks) or clinopyroxene (clinopyroxene-bearing volcanic rocks) as the main mafic mineral. Even though both types coexist, the amphibole-bearing volcanic rocks are the most common.

The rocks are mainly composed by plagioclase (40-60% of the phenocryst population), whose phenocrysts are euhedral to subhedral and can be up to 3 mm in size (Fig. 3a, b). They commonly display optical zoning, signs of resorption and disequilibrium margins, as well as synneusis, sieve textures and albitic rings and rims (the albitic compositions are shown by sample G2-63; Fig. 3a, b). The rocks contain either amphibole phenocrysts (40-10% of the phenocryst assemblage) with phenocrysts of plagioclase and/or biotite and clinopyroxene (amphibole-bearing rocks; Fig. 3a, c) or clinopyroxene phenocrysts associated with plagioclase phenocrysts and tiny amphibole

197 microphenocrysts (clinopyroxene-bearing rocks; e.g. G3-157; Fig. 3b, d). Table 1-
198 Appendix summarizes mineral assemblages.

199 Amphibole-bearing rocks are characterized by a subhedral light green to brown
200 pleochroic amphibole (Fig. 3c) with occasional Fe-Ti slight oxide rims and common
201 polysynthetic twinning. Optical zoning is commonly seen, as in samples G2-63 and T1
202 (Fig. 3c, e). Phenocrysts are commonly preserved as whole crystals, however, in some
203 samples they are skeletal (e.g., G3-134; Fig. 3f). Where present, biotite is brown
204 pleochroic and may be altered to iron oxides. Clinopyroxene occurs as relict cores in
205 amphibole phenocrysts (e.g., sample G3-134).

206 Clinopyroxene-bearing rocks contain ~20% of small euhedral clinopyroxene
207 phenocrysts (sample G3-157; Fig. 3b, d). Coexisting amphibole occurs only as scarce
208 brown and pleochroic microphenocrysts (Fig. 3d; G3-157).

209 Groundmass textures of both varieties are microcrystalline, sometimes pilotaxitic or
210 hyalopilitic, composed of microliths of the same mineral assemblages as the
211 phenocrysts (Fig. 3). Accessory minerals are titanomagnetite, titanite and apatite. The
212 latter occurs as euhedral, stubby apatite crystals, either isolated in the groundmass or as
213 inclusions in plagioclase phenocrysts. Interstitial glass is commonly replaced by sericite
214 and clays. All samples are moderately altered to a propylitic assemblage given by
215 chlorite, carbonate, secondary titanite, quartz, epidote, albite and opaque minerals. The
216 alteration is mainly found in the groundmass while phenocrysts are essentially fresh,
217 except the biotite, whose phenocrysts appear replaced by chlorite and opaque minerals
218 (e.g., G2-63), so that no fresh biotite analyses could be obtained.

219 **6. BULK ROCK GEOCHEMISTRY**

220 Major element geochemistry suggests that the Lonco Trapial volcanics are medium
221 potassium andesites to dacites, and also trachydacites (Fig. 4a,b) with SiO_2 between

222 58.57 and 63.17%, K_2O < 2.30%, Al_2O_3 > 16.12%, and Na_2O varying from 3.86 to
223 5.27% (anhydrous basis; Table 1-Appendix). All are metaluminous (average ASI index
224 0.86; Table 1-Appendix) and silica oversaturated, having quartz and hypersthene,
225 apatite and ilmenite in their CIPW normative compositions. It should be noted that the
226 classification based on immobile element ratios of (Winchester and Floyd, 1977)
227 essentially agrees with the major element classification (Fig. 4c).

228 In the TAS diagram, rock compositions cluster around the alkaline-subalkaline
229 boundary (Fig. 4a). They are calc-alkaline magmas in the sense of Miyashiro (1974,
230 Fig. 4d). Their FeO_t/MgO vs SiO_2 content is variable, and their CA/TH index (Hora et
231 al., 2009) is between 0.93 and 2.23, so they belong to medium- to low-Fe calc-alkaline
232 series (Arculus, 2003; Table 1-Appendix, Fig. 4d).

233 Their chondrite-normalized REE patterns (McDonough and Sun, 1995) have negative
234 slopes, being variably enriched in LREE and depleted in HREE [$(La/Yb)_N$=14-7] (Fig.
235 5a, Table 1-Appendix) and subtle Eu anomalies, which can be either slightly negative or
236 positive (Eu/Eu*= 1.1-0.9; Table 1-Appendix). The fractionation mainly involves the
237 light and middle REE [$(La/Dy)_N$=10-4], whereas the heavy REE pattern is rather flat or
238 slightly positive from Ho to Lu [$(Ho/Lu)_N$=1.3-0.95] causing a concave up curvature
239 (Fig. 5a, Table 1-Appendix). Decreasing Dy/Yb with increasing SiO_2, and the
240 decreasing Dy/Yb and Dy/Dy* (Dy*=value interpolated; Davidson et al., 2013; Fig. 5c,
241 Table 1-Appendix) with differentiation, which is roughly orthogonal to the depletion-
242 enrichment trend would indicate that the rocks are cogenetic according to Davidson et
243 al. (2013) (Figs. 5b, 5c).The concave up shape of REE patterns, the decreasing
244 $[Dy/Yb]_N$ (1.71-1.25) with increasing SiO_2 (Fig. 5b), and the low Dy/Dy* values
245 (Dy*=value interpolated; Davidson et al., 2013; Fig. 5c, Table 1-Appendix) point out

the role of amphibole±clinopyroxene fractionation and the absence of garnet, fractionated or residual in the melting source (Davidson et al., 2013).

Trace element patterns show a general behavior that is typical of rocks of the calc-alkaline series, with LILE enrichment, negative Nb and Ta anomalies (except Ta in sample G3-134) and with a positive spike in Pb (Fig. 5d). The Lonco Trapial samples also show lesser contents of Ti, Y and Yb than N-MORB (Sun and McDonough, 1989, Fig. 5d). Samples G3-157 and G3-134 are richer in Th, U, Zr, Ti, Y, REE and also in Ta (in sample G3-134) with respect to the other samples, showing contents similar to those presented by alkaline rocks. This affinity also arises from the chemical composition of their phenocrysts, as will be shown below.

7. MINERAL COMPOSITIONS

Representative electron microprobe analyses of plagioclase, amphibole, clinopyroxene and titanomagnetite are presented in Table 2-Appendix, ICP-MS analyses of amphiboles from representative samples are presented in Table 3-Appendix and EDS analyses of amphiboles are shown in Table 4-Appendix.

7.1. Amphibole major and trace element compositions

Amphibole structural formulas were calculated on the basis of 23 O after the method of Dale et al. (2005) and with all Ca in the M4 site (Table 2a-Appendix). Amphibole compositions are calcic, with $Fe_t/(Fe_t+Mg)$ in the 0.30-0.47 range and have moderate to high TiO_2 contents (0.85 to 1.65% and 0.10 to 0.17 a.p.f.u. in amphibole-bearing dacite G2-63; 3.25 to 3.77% and 0.36-0.42 a.p.f.u. in clinopyroxene-bearing trachydacite G3-157). The $Fe^{3+}/(Fe^{3+}+Fe^{2+})$ ratio is moderate in the amphibole-bearing dacite G2-63 (between 0.45 and 0.25) and low in clinopyroxene-bearing trachydacite G3-157 (between 0.08 and 0.15). Amphiboles in amphibole-bearing volcanic rocks (G2-63) are tschermakite (mostly the cores) to magnesiohornblende (Fig. 6a), whereas in

clinopyroxene-bearing volcanic rocks (G3-157) they are magnesiohastingsite (Fig. 6b). Amphibole compositions in the samples analyzed by EDS (all amphibole-bearing volcanic rocks) are more varied but similar to the EMP analyses. They are all classified as magnesiohornblende (Fig. 6a).

In all amphiboles, the charges due to the introduction of the Al tetrahedral site occupancy seems to be balanced by a combination of the edenitic and tschermakitic substitutions (Fig. 6c). In some samples (G3-157 and JZ6-4) the Al^{IV} in amphibole is slightly controlled by TiO_2 content (Fig. 6d). The amphiboles show a general normal zoning pattern where the core is richer in Al and Ti and poorer in Si and Fe than the rim (Fig. 1-Appendix).

All amphiboles present moderate REE abundances and slightly negative europium anomalies (Fig. 7a; Eu/Eu* ranging from 0.69 to 0.89). Amphiboles in samples G2-63 and T1 have similar REE patterns with a convex upward shape, as amphiboles are depleted in light REE and enriched in middle REE (Fig. 7a). In contrast, the amphibole from sample T0 shows upward concavity in the heavy REE and a less marked convex upward shape in the light REE (Fig. 7a). In turn, sample G3-134 has a steeper heavy REE slope and a less pronounced Eu anomaly (Fig. 7a). Incompatible trace element patterns of the amphiboles normalized to the Primitive Mantle (Sun and McDonough, 1989) display positive Ba, Nb, Pr, Ce, Nd and Sm anomalies, and negative Rb, Sr, Zr, U and Th anomalies (Fig. 7b). The amphiboles from samples G3-134 and T0 have greater content of Th, U, Pb, and Yb and Lu (only sample T0 shows the last two; Fig. 7b).

7.2. Plagioclase, clinopyroxene and titanomagnetite compositions

Plagioclase compositions were calculated on the basis of 32 O (Table 2b-Appendix). Plagioclases in the amphibole-bearing dacite (G2-63) are mainly andesine from cores

(An46) to rims (An30), with some rounded and resorbed labradorite cores (An55), and internal concentric zones or outer rims of albite (An3-1) (Fig. 2a,b-Appendix; Table 2b-Appendix). Plagioclase compositions in the clinopyroxene-bearing trachydacite G3-157 range from labradorite-andesine (An55-37) in the cores to andesine-oligoclase in the rims (An46-29; Fig. 2c-Appendix, Table 2b-Appendix).

Clinopyroxene analyses from the clinopyroxene-bearing trachydacite G3-157 are presented in Table 2c-Appendix and compositions were calculated on the basis of 6 O. According to Ca (0.80-0.85 a.p.f.u.), Mg (0.83-0.87 a.p.f.u.), Fe^{2+} (0.25-0.29 a.p.f.u.) and Na (0.017-0.028 a.p.f.u.) contents, they are augite (Morimoto, 1988) with Mg# rather homogeneous (~0.73-0.77). As in the amphiboles of this sample, the content of Al^{IV} is balanced by the content of TiO_2 (Fig. 6e).

Titanomagnetite belongs optically to the stage 1 of homogeneous TiO_2-rich magnetite or to stage 2 of magnetite-enriched solid solutions with a small number of exsolved ilmenite lamellae (Haggerty, 1991). Titanomagnetite compositions, calculated on the basis of 4 O (Table 2d-Appendix), correspond to TiO_2-rich magnetites ($Y=Fe^{+3}$ is greater than 75%, and Ti content of the crystals is generally higher than 0.2 a.p.f.u.). When plotted in the triangular diagram of FeO, TiO_2, Fe_2O_3 (Fig. 6f) titanomagnetite compositions represent the solid-solution between magnetite and ülvospinel. These solid solutions exist above 600ºC (Buddington and Lindsley, 1964).

8. DISCUSSION

8.1. Geochemical signature of Lonco Trapial magmas

The andesites, dacites and trachydacites of Lonco Trapial Formation are calc-alkaline rocks (Fig. 4a). When compared to the Primitive Mantle, the rocks show, as other calc-alkaline suites, pronounced enrichment in Sr, Ba and Pb and strong depletion in Nb and

Ta (Fig. 4d). Moderate LILE enrichment, typical of calc-alkaline magmas, is also shown in the chondrite-normalized spider diagram (Fig. 5a). Trace element ratios are characteristic of calc-alkaline magmas, given by high La/Ta (La/Ta > 25 except G3-134: Table 1-Appendix), Ba/Nb>40, La/Nb>1 and Th/Nb>0.5 and low Nb/Zr (<0.05, except G2-63) and Ce/Pb<20 ratios (Table 1-Appendix). Similarly, the samples display decreasing Dy/Dy* and Dy/Yb trends with differentiation, orthogonal to the MORB trend (which goes from depleted to enriched light REE, Fig. 5c) characteristic of calc-alkaline magmas (Davidson et al., 2013).

Even though the calc-alkaline signature of Lonco Trapial lavas is strong, some intraplate characteristics are also present. Whole-rock trace element ratios show that some samples present Ta/Hf > 0.15 which is distinctive of intraplate magmas (e.g., Kay et al., 2006). Sample G3-134 has a Dy/Yb ratio (2.6) which is close to the OIB field (Fig. 5c). However, the rest of the samples have low Dy/Yb ratios (2.3-1.9) which are characteristic of calc-alkaline magmas.

As phenocrysts of volcanic rocks would have formed in the early stages of the magmatic history, any inference about the chemistry of the magma coming from them would be useful. When compared with amphiboles of different tectonic settings, the Lonco Trapial amphiboles coincide with those of calc-alkaline rocks (Fig 8; Demény et al., 2012). However, mineral chemistry proves to be particularly sensitive in unraveling some alkaline affinity of the Lonco Trapial lavas. For example, TiO_2 content in amphiboles and clinopyroxenes is a good indicator of magma alkalinity (Molina et al., 2009). Amphibole from the clinopyroxene-bearing trachydacite G3-157 and of the amphibole-bearing volcanic rocks G3-134 and JZ6-4 have crystallized from subalkaline trachytoid to alkaline magmas (Fig. 9a-d), whereas the amphiboles from the amphibole-bearing volcanic rocks G2-63, T0 and T1 crystallized mostly from subalkaline magmas

(Fig. 9a-d). Consistently, clinopyroxenes of the clinopyroxene-bearing trachydacite G3-157 also crystallized from magmas transitional between subalkaline and alkaline (Molina et al., 2009) (Fig. 9e). These clinopyroxenes also crystallized from calc-alkaline orogenic magmas transitional to intraplate magmas according to the diagrams of Le Bas (1962) (Fig. 9f), Nisbet and Pearce (1977) (Fig. 9g) and Leterrier et al. (1982) and (Fig.9h-i).

We interpret that Lonco Trapial lavas were erupted within widespread rifting conditions. In addition, they are located in the rear arc of a paleo-subduction zone represented by the Subcordilleran Plutonic Belt. The origin of the Lonco Trapial magmas can be ascribed to two different settings (or combinations): 1) a rifting phase, where the mantle source rocks were affected by previous subduction processes and 2) a rifting phase, where the calc-alkaline signature is inherited by assimilation of crustal rocks (a mixed source). Around Gastre, two different previous orogenic cycles could have produced mantle metasomatism in the area. These cycles produced the Late Paleozoic granites of the Gondwanide orogeny (López de Luchi and Cerredo, 2008; Pankhurst et al., 2006, Rapela et al., 1991; Rapela and Pankhurst, 1992), and the pre-rifting Late Triassic granites of the Central Patagonian Batholith (Rapela et al., 1991; Rapela and Pankhurst, 1992; Pankhurst et al., 2006; Zaffarana et al., 2014; 2017).

Crustal contamination, in turn, is suggested by the Nb/Ta ratios of the Lonco Trapial lavas (average ~8; Table 1-Appendix). Nb/Ta ratios are lower than in arc-related basalts and OIB (arc basalts have an average Nb/Ta of ~15; Munker et al., 2004; whereas the continental crust has a Nb/Ta reference value of 11.4; Rudnick and Gao, 2003). Therefore, Nb/Ta ratios suggest crustal assimilation in the origin of the magmas (e.g. see Moreno et al., 2016, for further discussion). The variation in the amphibole multielemental pattern (Fig. 7b) would support mixing of magmas of different origin

(mantle and crustal generated magmas) in the genesis of the Lonco Trapial volcanic rocks. Even though the corroded appearance of some of the amphiboles can be due to decompression, it could also be attributed to magma mixing, as well as the disequilibrium textures shown by the plagioclases. Furthermore, the Middle Jurassic andesites associated with the Cañadón Asfalto rift basin show field, petrographic and geochemical characteristics attributable to crustal assimilation (Bouhier et al., 2017). These authors explained the arc signatures of Lonco Trapial magmas as due to assimilation of crustal rocks supported by the recognition of zircon xenocrysts with Permian and Middle- Upper Triassic ages (281.3 Ma, 246.5, 218.1, and 201.3 Ma) within these volcanic rocks. The isotopic data from Dejonghe et al. (2002) also suggested that the Lonco Trapial magmas are a mixture of mantle and crustal-derived magmas.

Other rock suites generated in extensional environments bear a calc-alkaline geochemical signature. For example, the Variscan appinites from Iberia (Bea et al., 2006; Molina et al., 2012; Scarrow et al., 2009), and the quartz-monzonites from the Katerina Ring Complex, southern Sinai, Egypt (Moreno et al., 2014; 2016). There, the magmatism was generated in a post-collisional regime, but in both cases the calc-alkaline signature suggests an important involvement of a continental crust component in the magmas. Nevertheless, metasomatism in the mantle source due to a previous subduction event shoud not be ruled out anyway.

8.2. Parental melt compositions, oxygen fugacity and fractionating phases

The amphiboles are products of crystallization in calc-alkaline magmas. The equilibrium magmatic conditions and melt composition are calculated from the spreadsheet Amp-TB.xls of Ridolfi et al. (2010) (Fig. 10a). The method also estimates the oxygen fugacity conditions of the melt (Fig. 8b). In the amphibole-bearing dacite

(G2-63), the amphibole cores coexisted with liquid of andesitic to dacitic composition (Fig. 10a, Table 2), while some rim compositions (G2-63) are in equilibrium with a melt of dacitic to rhyolitic composition (Fig. 10a). In turn, core and rim compositions of the small amphibole phenocrysts of the clinopyroxene-bearing trachydacite G3-157 crystallized in equilibrium with melts of dacitic composition (Fig. 10a). The amphiboles from the two samples crystallized in high fO_2 conditions between the NNO and NNO + 2 curves (Fig. 10b; Ridolfi et al., 2010), consistent with oxygen fugacity values inferred for calc-alkaline magmas (ΔNNO from -1 to +3; e.g. Gill, 1981; Behrens and Gaillard, 2006). The low $Fe_t/(Fe_t+Mg)$ ratios also indicate that amphiboles crystallized at high-fO_2 conditions (Anderson and Smith, 1995), in consonance with the presence of titanomagnetite as the main oxide phase (see below, Fig. 10c).

Amphibole/melt partition coefficients for La, Yb, Sm, Eu and Gd for different kinds of melts are available in the literature (see overview in Tiepolo et al., 2007). Hornblende partition coefficients strongly vary with melt compositions (Sisson, 1994). To minimize this problem, the $[La/Yb]_N$ and the Eu/Eu* anomaly of the melt in equilibrium with the amphiboles was estimated using Kd for different melt compositions and then it was compared with the whole-rock compositions (Table 3). Although it is difficult to get precise estimations of melt $[La/Yb]_N$ ratios and Eu/Eu* anomalies due to the large scattering in Kd values, there are some tendencies that can be analyzed. For instance, in the more evolved rocks, the $[La/Yb]_N$ ratio calculated for interstitial melts is lower than the whole-rock ratio, implying that the light REE become more compatible than the heavy REE. This is a fact that cannot be ascribed to amphibole fractional crystallization, and which can be attributed to the fractional crystallization of titanite, which is a mineral phase which concentrates light REE (Bea, 1996).

Assuming a theoretical dacitic composition for the interstitial melt, which is reasonable, because after amphibole and plagioclase crystallization the melt becomes more acidic than the parental melt, a strong Eu fractionation occurs with respect to Sm and Gd. This would imply plagioclase saturation of the magma (Table 2). The Eu/Eu* values close to 1 in the whole-rock (Table 2) would suggest a lesser plagioclase fractionation, which is consistent with plagioclase behavior in andesitic melts rich in water (Sisson and Grove, 1993; Molina et al., 2009), where it decreases its appearance temperature by >100 ºC (Sisson and Grove, 1993). This further agrees with the REE modelling, which suggests that plagioclase crystallization took place with ongoing crystallization. Amphibole REE patterns do show negative Eu anomalies (Fig. 7a), that could be ascribed either to concomitant plagioclase fractionation (see, for example, Schnetzler and Philpotts, 1970), or to the low Kd for Eu that amphibole has in andesitic and basandesitic melts (i.e. Tiepolo et al., 2007 and references therein). These REE patterns in amphibole could also be ascribed to mixing with, or assimilation of crustal material (that already had fractionated plagioclase) before amphibole crystallization.

Amphibole ± clinopyroxene fractionation during differentiation was suggested by the decreasing $[Dy/Yb]_N$ with increasing SiO_2 (Fig 5b), and by the low Dy/Dy*, and the trend of decreasing Dy/Dy* with decreasing Dy/Yb (with increasing SiO_2; Davidson et al., 2013, see Fig. 5c). Amphibole fractionation, together with crustal contamination, can be another cause of the low Nb/Ta ratio of the Lonco Trapial magmas (average ~8; Table 1-Appendix, Li et al., 2017; see the previous section).

Apatite fractionation is another cause of middle REE fractionation in metaluminous magmas (Bea, 1996). The fractionation of this mineral is also suggested by the high apatite saturation temperatures which were obtained from the amphibole-bearing volcanic rocks (Table 3, see below). The low apatite saturation temperatures in the

clinopyroxene-bearing trachydacite G3-157 contrast with the presence of abundant stubby apatite crystals in the groundmass of this sample. This would suggest that even though the liquid represented by the whole-rock would not be saturated in apatite, the interstitial liquid in equilibrium with amphibole would have reached apatite saturation temperatures. In addition, the compatible behavior of P (not shown) would indicate apatite fractionation. No zircon fractionation could be inferred from zircon saturation temperatures (see below), which are very low and close to the solidus in amphibole-bearing and well as in clinopyroxene-bearing volcanic rocks, nor from the petrographic analysis (no zircon crystals could be observed in the rocks). Therefore, the compatible character of Zr (not shown) can be ascribed, then, to amphibole crystallization (Bea et al., 2006).

All in all, co-crystallization of amphibole, plagioclase, titanite, titanomagnetite and apatite is suggested by amphibole depletion in Sr, Zr, U, Th and Ti (with some exceptions, see Fig. 7b) and by the compatible character of Zr and P. It is therefore concluded that differentiation processes in the Lonco Trapial volcanic rocks were controlled by a combination of amphibole, clinopyroxene, plagioclase, titanite, titanomagnetite and apatite fractionation.

8.3. Magma storage temperatures and pressures

Calc-alkaline andesites and dacites commonly show amphiboles with complex zoning and reaction textures such as the ones present in Lonco Trapial volcanic rocks. Reasonable estimations of environmental (P, T, fO2) and compositional parameters (liquid composition in equilibrium with amphibole) can be recovered from amphiboles of this kind by careful selection of mineral compositions (see for example Blundy et al., 2006; Kiss et al., 2014; Zhang et al., 2017). It should be taken into account, besides, that

amphiboles with reaction textures provide constraints on the earlier (pre-breakdown) equilibrium conditions (Ridolfi et al., 2008).

Magma storage temperatures were calculated with different geothermometers that are based on amphibole-plagioclase compositions (Holland and Blundy, 1994, expression B), amphibole compositions (Ridolfi et al., 2010; Ridolfi and Renzulli, 2012; Putirka, 2016), melt compositions (Molina et al., 2015; Putirka, 2016), or on zircon (Harrison and Watson, 1983; Boehnke et al., 2013) and apatite compositions (Harrison and Watson, 1984). Individual results are presented in Tables 1-3 in the Appendix, and a summary is presented in Table 3.

Temperatures calculated with the calibrations of Ridolfi et al. (2010), Ridolfi and Renzulli (2012) and Putirka (2016) (Fig. 10d) broadly agree (Table 3). Temperatures obtained with the calibration of Putirka (2016) shown in Figure 10d are considered the most accurate because this geothermometer uses the most complete dataset of experimental amphiboles. In all samples, these temperatures are between ~820 and 970°C (Table 3), in agreement with amphiboles crystallized from andesitic to dacitic melts not in equilibrium with quartz (Ridolfi et al., 2010). Taking the three temperature calibrations into account, amphibole cores in sample G2-63 crystallized at ~ 869-916 ºC with an average of 895 ºC, whereas amphibole rims crystallized at ~825-865 ºC with an average of 850 ºC (Table 3). The higher temperatures in the amphibole microphenocrysts of the clinopyroxene-bearing volcanic rocks (cores ~960-1017 ºC, and rims ~929-1000 ºC; Table 3) are due to higher Ti contents, in agreement with their more primitive and alkaline character (Molina et al., 2009).

The geothermometer based on amphibole-plagioclase equilibrium of Holland and Blundy (1994) was applied for samples G2-63 and G3-157. Temperatures for amphibole cores and plagioclase cores for sample G2-63 are around 857°C and around

948°C for sample G3-157 (Table 3). These temperatures generally coincident with the amphibole-only temperatures of Ridolfi et al. (2010), Ridolfi and Renzulli (2012) and Putirka (2016) geothermometers (Table 3), although they are a bit lower probably due to calibration problems (Blundy and Cashman 2008).

Liquid-only temperatures for amphibole-saturated magmas of Molina et al. (2015) and Putirka (2016) are slightly higher than the temperatures calculated from amphibole phenocrysts. The composition of the liquid was estimated by the whole-rock composition. The obtained temperatures range from 960 to 1052 ºC (Table 3), they are compatible with the stability field of amphibole in subalkaline liquids (see Fig. 14 in Molina et al., 2009 and Fig. 9 in Kiss et al., 2014). These results are concordant with amphibole-saturated parental melts. These temperatures are higher than the temperatures estimated from amphibole-only geothermometers, even higher than the temperatures estimated from the cores of the amphibole phenocrysts (Table 3). The reason for this would be that these liquid-only temperatures may be representative of a liquid saturated in amphibole, but this amphibole would not be the one forming the phenocrysts, which would be in equilibrium, instead, with a liquid of a more evolved composition.

Apatite saturation temperatures calculated for the amphibole-bearing volcanic rocks are close to the liquid-only temperatures, suggesting apatite saturation in parental melts consistent with the presence of apatite crystals in the groundmass. The apatite saturation temperatures in the most primitive sample (clinopyroxene-bearing trachydacite G3-157) are significatively lower than the amphibole-only and the liquid-ony temperatures. The low zircon saturation temperatures close to the solidus in amphibole-bearing as well as in clinopyroxene-bearing volcanic rocks suggest that the magma was not saturated in zircon (Table 3).

517 The composition of the amphiboles is compared with amphiboles experimentally
518 crystallized at different temperature and pressure conditions in Figure 10e (Kiss et al.,
519 2014). The amphiboles of Lonco Trapial generally agree with the field of experimental
520 amphiboles crystallized between 800 and 900 ºC, which is consistent with temperatures
521 predicted by the Putirka (2016) and Ridolfi et al. (2010) geothermometers (Table 3).

522 We estimated crystallization pressures using the amphibole-only geobarometers of
523 Ridolfi et al. (2010) and Ridolfi and Renzulli (2012) (equation 1d), which is considered
524 the most accurate (Molina et al., 2015) and the amphibole-plagioclase barometer of
525 Molina et al. (2015). Only the amphibole-bearing dacite G2-63 was suitable for the
526 geobarometer of Molina et al. (2015) because the amphiboles of the clinopyroxene-
527 bearing trachydacite G3-157 were rejected because they had Al^{vi} <0.05. Pressures
528 calculated with the Molina et al. (2015) geobarometer range from 8 to 5 kbar (average
529 7.6 kbar at T1, Table 3) for cores and from 2-4 kbar (average 3.5 kbar at T1, Table 3)
530 for rims. The amphibole-plagioclase barometer of Anderson and Smith (1995) was used
531 with the temperature calculation of Holland and Blundy (1994) considering amphibole
532 and plagioclase core compositions of sample G2-63. Results show pressures around
533 6.29 kbar, which are mostly within the range of core pressures obtained with the Molina
534 et al. (2015) amphibole-plagioclase barometer.

535 For sample G2-63, pressures calculated with the calibrations of Ridolfi et al. (2010) are
536 around 7.4 kbar for the cores and around 2.2 ± 0.4 kbar for the rims (Table 3). For the
537 same sample, pressures calculated with the calculation of Ridolfi et al. (2012) are
538 around 1.65 ± 2.5 kbar for the rims (Table 3). Amphibole-plagioclase equilibrium
539 pressures are around 6.29 kbar using the iteration geobarometer of Anderson and Smith
540 (1995) with core compositions in both minerals. In addition, we performed the
541 amphibole-plagioclase geobarometric calculation of Molina et al. (2015), and their

542 pressures were comprised within 8 and 5 kbar for the cores and between 2 and for kbar
543 for the rims (Table 3). The general consistency of the pressures calculated for the cores
544 and rims of the amphibole-bearing dacite G2-63 suggests that equilibrium conditions
545 were reached during the crystallization history of the amphibole-bearing volcanic rocks.

546 In turn, for the clinopyroxene-bearing trachydacite G3-157, the temperature-dependent
547 geobarometer of Putirka (2008; equation 32a) was employed, as it contains
548 clinopyroxene phenocrysts and small amphiboles microphenocrysts. For this
549 calculation, the temperatures obtained from cores of amphiboles based on the pressure-
550 independent geothermometer of Putirka (2016) were used. As a result, the calculated
551 pressures are around 2 kbar (Table 3). The amphibole-plagioclase barometer of
552 Anderson and Smith (1995) was also used in this sample, considering amphibole and
553 plagioclase core compositions, and using the temperature calculation of Holland and
554 Blundy (1994). A pressure of 2.51 kbar was therefore obtained (Table 3). The
555 amphibole-only geobarometer of Ridolfi et al. (2010) also gave a pressure around 2
556 kbar for cores and rims (Table 3). In this sample there is also a consistency in the
557 obtained pressures for cores and rims (with the clinopyroxene-only geobarometer of
558 Putirka (2008), with the geobarometer of Ridolfi et al. (2010) and with the
559 geobarometer of Anderson and Smith (1995), Table 3). In addition, there is a
560 consistency within the pressures of cores and rims of sample G3-157 with the pressures
561 obtained for the rims of sample G2-63 (within error). This consistency may further
562 suggest equilibrium conditions during the crystallization of the clinopyroxene-bearing
563 volcanic rocks.

564 It must be observed, though, that in sample G3-157, higher pressures around 3-4 kbar
565 are obtained with the equation 1.d of Ridolfi and Renzulli (2012) (Table 3) and with the
566 Al-in-hornblende geobarometers. However, as the latter geobarometers tend to

overestimate the pressures, especially in quartz-undersaturated magmas because amphibole tends to have lower Si content thus increasing Al^{IV} occupancy (see Hammarstrom and Zen, 1986), it is considered that the real pressures for this sample should be around 2 kbar.

8.4. General tectonic interpretation of thermobarometric and geochemical data

Crystallization temperatures for the amphibole- and clinopyroxene-bearing volcanic rocks of the Lonco Trapial Formation are constrained around 826 and 1017 °C (Table 3). These temperatures are typical for magmas of intermediate composition (e.g. Rutherford and Devine, 2008), and the temperatures are below the maximum stability of amphibole in primitive magmas (around 1050 ºC; Pichavant et al., 2002; Grove et al., 2003; Barclay and Carmichael, 2004; Adam et al., 2007; Krawczynski et al., 2012; Simakin et al., 2012).

Pressures estimated for the amphibole rims in the amphibole-bearing volcanic rocks are comprised between 2 and 4 kbar. In addition, pressure estimations for the amphibole microphenocrysts (cores and rims) in the clinopyroxene-bearing volcanic rocks are around 2 kbar (Table 3). These amphiboles would have crystallized in equilibrium with plagioclase within the upper crust (between 7 and 15 km, approximately, using a geothermal gradient of 3.7 km/kbar). In the amphibole-bearing volcanic rocks, the cores of the amphiboles would record a previous history, and they would have crystallized at a different pressure around ~7-8 kbar which would correspond to ~22- 26 km.

Pressures around 2-8 kbar in the amphibole cores and rims of the amphibole-bearing volcanic rocks are consistent with whole-rock geochemical data, as the host-rock has no fractionated heavy REE (Yb < 2.4, $[La/Yb]_N$ between 7 and 14, Table 1-Appendix), and

590 the decreasing Dy/Yb trend with silica is consistent with amphibole and/or
591 clinopyroxene (and no garnet) at the source or as a fractionating phase (Fig. 5b,c).

592 The different pressures calculated for the cores and rims of the amphibole-bearing
593 volcanic rocks would suggest a polybaric history of crystallization along a transcrustal
594 magmatic reservoir (see review of transcrustal magmatic systems in Cashman et al.,
595 2017) for Lonco Trapial andesites, dacites and trachydacites (Fig. 11b). Sr, Nd and Pb
596 isotopic data of Bouhier et al. (2017) support crustal and mantle contribution to the
597 Jurassic magmas of Lonco Trapial Formation. The andesitic to dacitic magmas, which
598 bear low Cr and Ni contents must have evolved from a mantle source. In summary, the
599 calc-alkaline signature of Lonco Trapial Formation andesites, dacites and trachydacites
600 could have been obtained either from a mantle source previously metasomatized by
601 earlier subduction processes (Late Paleozoic and Late Triassic; Proserpio, 1978; Rapela
602 and Pankhurst, 1992; Pankhurst et al., 2000) or, alternatively, by crustal contamination.
603 However, the role of crustal contamination should have been strong, as is evidenced by
604 the Nb/Ta ratios and by the isotopic data of Bouhier et al. (2017).

605 The Lonco Trapial lavas constitute the basement of the Early Jurassic Cañadón Asfalto
606 basin, as it overlies the syn-rift deposits of the Las Leoneras Formation (Cúneo et al.,
607 2013; Fig. 1a). As no marine ingressions were registered on this basin, the crust should
608 not have been thinner than 35 km (i.e. Ramos et al., 2004). It is therefore inferred that
609 the Early Jurassic rifting could have developed on a previously thickened crust (around
610 50-60 km), probably inherited from the Late Paleozoic Gondwanic Orogenic Cycle (i.e.
611 Pankhurst et al., 2000). The crust would have thinned in the Early Jurassic (during V1
612 volcanic event) to ~35 km. Therefore, the obtained pressures are coherent with regional
613 geological constraints. The present-day Moho depth in Gastre is around 44 km, as is
614 inferred by the crustal model GEMMA obtained from inversion of gravimetric data

(Reguzzoni and Sampietro, 2015; Fig. 11c-d). The greater depth found today would have been reached by thermal subsidence after the rifting period (by deposition of younger material in the Gastre basin, see for example Bilmes et al. 2013) and during Mid-Cretaceous upper plate contraction (Zaffarana et al. 2018; Echaurren et al., 2016; 2017).

9. CONCLUSIONS

The Early Jurassic volcanic rocks of the Lonco Trapial Formation erupted coevally with widespread extension during the early stages of Gondwana break-up. The andesites, dacites and trachydacites can be divided into two main types: amphibole-bearing and clinopyroxene-bearing (volcanic rocks with either amphibole or clinopyroxene as the main mafic mineral), though the amphibole is the most common mafic phase. They represent calc-alkaline magmas; nevertheless, a mild alkaline affinity arises from some whole-rock trace elements content and from mineral chemistry (amphibole, clinopyroxene and titanomagnetite compositions). The calc-alkaline signature of the Lonco Trapial magmas can reflect a mantle source metasomatised by a previous subduction processes and/or a significant assimilation of crustal rocks (the latter being particularly supported by the isotopic data from Bouhier et al., 2017).

Trace element data in amphiboles together with whole-rock trace element data suggest that the magmatic evolution of the Lonco Trapial magmas was governed by a combination of amphibole, clinopyroxene, plagioclase, titanite, titanomagnetite and apatite fractionation. A melt of andesitic to dacitic composition was inferred to be in equilibrium with the amphibole cores, whereas a melt of dacitic to rhyolitic composition was inferred to be in equilibrium amphibole rims. Amphibole and apatite crystallization would have predominantly controlled the fractionation of the middle REE.

The cores of the amphiboles in the amphibole-bearing volcanic rocks of the Lonco Trapial Formation crystallized at a temperature ranging from 869 to 916 °C, and the rims at a temperature ranging from 826 to 867 °C and at predominantly shallow to intermediate depths (2-8 kbar, ~7-26 km). The clinopyroxene-bearing volcanic rocks would have crystallized at higher temperatures, between 929 and 1017 ºC, consistent with their more primitive character. Oxygen fugacity conditions were high, in concordance with presence of titanomagnetite in some samples. The crystallization pressures of Lonco Trapial magmas agree with regional geological observations which suggest that the Moho depth in the Gastre area did not surpass 35 km in Early Jurassic times.

ACKNOWLEDGEMENTS

This work was financed with PIP CONICET 112-200901-00766, PICT 2014-1394 and with the Torandes Project (CGL2012-38396-C03) from the Plan de I+D+i Español with UE-FEDER funds. We thank Gerhard Wörner for the analyses of the amphiboles by ICP-MS at the GZG, University of Göttingen (Germany). We thank Andrés Cuesta and Miguel Ángel Fernández for their help in the analysis by electron microprobe at the Technical-Scientific services of Oviedo University (Spain). We greatly thank José Francisco Molina, Michel Grégoire and Kelly Russell for their great help with the correction of an earlier version of this manuscript. We are especially grateful to Romina Sulla for reviewing the English text.

FIGURE CAPTIONS

Figure 1: Regional and local geological frame of the Lonco Trapial Formation volcanic rocks. A) Early to Middle Jurassic rocks of in the North Patagonian Massif. The gray

663 area in Fig. 1A corresponds to the sampling area of Fig. 1B. The ages correspond to (1)
664 Pankhurst et al. (1993) (2) Gordon and Ort (1993) (3) Pankhurst y Rapela (1995) (4)
665 Féraud et al. (1999) (5) Franzese et al. (2002) (6) Sato et al. (2004) (7) Rapela et al.
666 (2005) (8) Zaffarana and Somoza (2012) (9) Cúneo et al. (2013) y (10) Benedini and
667 Gregori (2013). B) Local map of the area of Gastre showing the distribution of samples
668 and the studies performed.

669 Figure 2: ^{40}Ar-^{39}Ar age spectrum and isochron obtained from single mineral grains from
670 the andesitic lava of the Lonco Trapial Formation of sample G2-63.

671 Figure 3: Petrography of the andesitic lavas of the Lonco Trapial Formation.
672 Photomicrographs taken under crossed polars and plane-polarized light. Yellow points
673 in (A), (B) and (C) mark the sites studied with the electron microprobe. A) Plagioclase
674 phenocryst with inner albitic rings, amphibole-bearing dacite G2-63. B) Plagioclase
675 phenocrysts with synneusis and complex zoning, clinopyroxene-bearing trachydacite
676 G3-157. C) Plagioclase, biotite and green amphibole phenocrysts in sample G2-63. D)
677 Clinopyroxene-bearing trachydacite G3-157 with clinopyroxene and plagioclase
678 phenocrysts and amphibole and titanomagnetite microphenocrysts. E) Detail of
679 optically zoned amphibole in the amphibole-bearing andesite T3. F) Detail of skeletal
680 amphibole phenocrysts. Amphibole-bearing andesite G3-134. Mineral abreviations after
681 Whitney and Evans (2010). Amp: amphibole, Pl: plagioclase, Cpx: clinopyroxene, Bt:
682 biotite, Mag: magnetite.

683 Figure 4: General geochemical classification of the Lonco Trapial lavas based on
684 whole-rock major and trace-element data. A) Total alkalis versus silica (TAS) diagram
685 with classification of the studied rocks. Alkaline-subalkaline dividing line after Irvine
686 and Baragar (1971). B) K_2O vs. silica diagram (Peccerillo and Taylor, 1976) showing
687 that the Lonco Trapial volcanics are medium- to high-K calc-alkaline magma series. C)

Trace element classification of Winchester and Floyd (1977). D) Plot of the Lonco Trapial volcanics relative to calc-alkaline and tholeiitic fields of Miyashiro (1974) and high-, medium- and low-Fe fields of Arculus (2003). Dashed lines indicate uniform CA/TH index (Hora et al., 2009).

Figure 5: Trace element composition of the Lonco Trapial andesitic lavas. A) REE pattern of the analyzed rocks normalized to chondrite. B) Negative trend in the [Dy/Yb]N vs. SiO_2 diagram indicative of amphibole fractionation (Davidson et al., 2013). C) Plot of Dy/Dy* vs. Dy/Yb with extended Dy/Yb scale to show fields for MORB and OIB (Davidson et al., 2013). The percentages in red above or below each sample represent their silica content. D) Primitive Mantle normalized multielemental plot. NMORB and OIB curves (Sun and McDonough, 1989) are shown for comparison, together with data from the Subcordilleran Plutonic Belt (SPB; Haller et al., 1999; Rapela et al., 2005), the present Southern Volcanic Zone (SVZ; Wörner et al., 1988) and of the andesites comprised within the Marifil Formation (Pankhurst and Rapela, 1995). Chondrite normalization was taken from McDonough and Sun (1995) and Primitive Mantle normalization was taken from Sun and McDonough (1989).

Figure 6: Geochemistry of the amphiboles, clinopyroxenes and titanomagnetites of the Lonco Trapial volcanics. A) and B) Classification diagrams of Leake et al. (1997). C) Al^{iv} vs. $Al^{vi}+Fe^{+3}+2Ti+$"A" graph, showing that nearly all amphiboles have a good relation of 1:1 between vertical and horizontal axes. This would suggest that charge compensation due to the introduction of Al^{iv} was accomplished by both the edenitic and tschermakitic substitutions. D) Occupancy Al in tetrahedral site versus TiO_2 content. E) Positive correlation between Al^{iv} and TiO_2 content in clinopyroxenes from sample G3-157. F) Compositional range of titanomagnetites within the $FeO-Fe_2O_3-TiO_2$ diagram (wt %).

713

714 Figure 7: Trace element composition of hornblendes from the amphibole-bearing
715 volcanic rocks from Lonco Trapial Formation. A) Chondrite-normalized REE diagram
716 (McDonough and Sun, 1995). B) Primitive Mantle normalized multielemental diagram
717 (Sun and McDonough, 1989).

718 Figure 8: Trace element ratios of amphiboles of the Lonco Trapial volcanics showing
719 that they broadly coincide with the field of amphiboles crystallized in calc-alkaline
720 magmas of the Carpathian-Pannonian Region (Demény et al., 2012). A) Plot of Th/Nb
721 vs. Ba/Nb. B) Plot of Th/Yb vs. Ba/Yb. C) Plot of Nb/U vs. Ce/Pb. D) Plot of Ce/Pb vs.
722 Nb. References: Black solid line: calc-alkaline rocks of the Carpathian-Pannonian
723 Region, grey solid line: amphiboles from gabbros and basalts from the Canary Islands
724 and dashed line: alkaline basalts of the Carpathian-Pannonian Region (Demény et al.,
725 2012).

726 Figure 9: Discrimination of magma type using amphibole and clinopyroxene data. A) to
727 D) Amphibole compositions of the Lonco Trapial volcanics plotted in the diagrams of
728 Molina et al. (2009). A) MgO vs. TiO_2. B) Na_2O/K_2O vs. TiO_2. C) Al_2O_3 vs. TiO_2. D)
729 TiO_2 vs. Temperatures calculated with Putirka (2016) geothermometer. E)
730 Clinopyroxene Ti vs Ca + Na content with fields taken from Molina et al. (2009). F)
731 Silica/alumina plot of the pyroxenes from LeBas (1962). G) Clinopyroxene plot of
732 discriminant functions F1 against F2 of Nisbet and Pearce (1977). VAB: volcanic arc
733 basalt, WPT: within-plate tholeiitic basalts, OFB: ocean-floor basalts, WPA: within
734 plate alkalic basalts. H) Discrimination diagram from Leterrier et al. (1982) showing
735 that the Lonco Trapial clinopyroxenes crystallized in orogenic basalts. I) Discrimination
736 diagram for clinopyroxenes (also from Leterrier et al., 1982), showing that

clinopyroxenes from sample G3-157 are similar to the ones crystallized in calcalkaline basalts.

Figure 10: Liquid compositions in equilibrium with amphibole and oxygen fugacities estimated from amphibole data and temperature data calculated from the amphiboles of the Lonco Trapial magmas. A) P-T diagram reproduced from Ridolfi et al. (2010) and B) logfO_2-T diagram reproduced from Ridolfi et al. (2010) with the spreadsheet Amp-TB.xls of Ridolfi et al. (2010). Error bars represent that the maximum logfO_2 errors are 0.4 log unit and the expected σ (22°C). In B) the graph shows the NNO and NNO + 2 curves from O´Neill and Pownceby (1993). C) Diagram of Anderson and Smith (1995) showing the effect of oxygen fugacity in hornblende compositions ($Fe_T/(Fe_T+Mg)$ vs. Al^{iv}). D) Compositional variation of the amphiboles (silica content) with the temperature calculated with Putirka (2016) geothermometer. Silica content calculated with the total Fe as FeO total (Excel spreadsheet of Putirka, 2016). E) Plot of Al^{iv} vs. Mg# showing the correlation of the Lonco Trapial magmas with experimental amphiboles crystallized under different conditions (fields taken from Kiss et al., 2014 and references therein).

Figure 11: Source of the Lonco Trapial andesitic magmas. A) Comparison of amphibole pressure data in the amphibole-bearing volcanic rocks obtained with the different calibrations. B) Interpretation of the magmatic system of the Lonco Trapial Formation bringing together all the available information. C), D) Current Moho depth estimated from inversion of gravimetric data (Reguzzoni and Sampietro, 2015). The lithological units are the same as in Figure 1a.

Table 1: General data of the samples collected: outcrop type, location, analyses performed, and age constraints. Mineral abbreviations after Whitney and Evans (2010).

761 Table 2: Estimation of melt composition in equilibrium with amphibole compositions
762 using hornblende/melt partition coefficients (Kd) for different melt compositions
763 (andesite, dacite and rhyolite). References: 1: Sisson (1994), 2: Bacon and Druitt
764 (1988), 3: Nagasawa and Schneltzer (1971) and 4: Matsui et al. (1977).

765 Table 3: Compilation of temperatures and pressures calculated for each sample. In the
766 amphibole-plagioclase barometer of Molina et al. (2015), T1 is the temperature obtained
767 with Putirka (2016) geothermometer (equation 5), whereas T2 is the temperature
768 obtained with Ridolfi and Renzulli (2012) geothermometer (equation 5). Standard
769 deviation of the data is signaled in the appropriate cases. Pressures in the cores of
770 sample G2-63 are signaled in italics and were left in the table to show that they are
771 higher than normal ones (they are not in equilibrium; see the text for further
772 explanations).

773

774 **Appendix**

775 Figure 1-Appendix: Scans across zoned amphibole from samples G2-63 (with electron
776 microprobe) and JZ6-4 (with EDS). In sample G2-63: profile 1 and 2:scans 0.6 mm
777 long, profiles 3 and 4: scans 0.4 mm long. In sample JZ6-4 the scan measures 0.6 mm
778 long.

779 Figure 2-Appendix: Plagioclase zoning profiles of the Lonco Trapial volcanics. A), B)
780 Profiles performed with electron microprobe in sample G2-63. Red points mark the
781 position of the albitic rings. C) Profile performed with electron microprobe in sample
782 G3-157.

783 Table 1-Appendix: Whole-rock geochemical data presented on anhydrous basis. CA/TH
784 index is after Hora et al. (2009), Dy/Yb* is after Davidson et al. (2013). Major oxides

785 are expressed on an anhydrous basis. The normalizations are performed with respect to
786 the chondrite of McDonough and Sun (1995). Temperature calculations performed with
787 different geothermometers are added (liquid-only from Molina et al., 2015; Zr-
788 saturation temperature from Harrison and Watson, 1983 and from Boehnke et al., 2013;
789 apatite-saturation temperature from Harrison and Watson, 1984).

790 Table 2-Appendix: Mineral compositions analyzed by electron microprobe. A)
791 Amphiboles (Amp). B) Plagioclases (Pl). C) Clinopyroxenes (Cpx). D)
792 Titanomagnetites (Mag). Mineral abbreviations after Whitney and Evans (2010). In
793 Table 2a-Appendix we added the results given by amphibole-only thermometers of
794 Ridolfi et al. (2010) (equation 1), Ridolfi and Renzulli (2012) (equation 2) and Putirka
795 et al. (2016) (equation 5). Also, we added the results from the geothermometers of
796 Ridolfi (2010) (equation 4) and Ridolfi and Renzulli (2012) (equation 1d). In Table 2c-
797 Appendix, results given by the temperature-dependent geobarometer in clinopyroxene
798 using the temperature of Putirka (2016) are added (equation 32a, Putirka 2008).

799 Table 3-Appendix: ICP-MS amphibole analyses. T1-1, T1-2, G3-63-1 and G2-63-2 are
800 different mineral separates from sample T1 and G2-63, respectively. Results given by
801 amphibole-only thermometers of Ridolfi et al. (2010) (equation 1), Ridolfi and Renzulli
802 (2012) (equation 2) and Putirka (2016) (equation 5) were added, as well as the results
803 from the geothermometers of Ridolfi et al. (2010) (equation 4) and Ridolfi and Renzulli
804 (2012) (equation 1d).

805 Table 4-Appendix: Amphibole compositions estimated with EDS (Cam, calcic
806 clinoamphibole).

807

808 **References**

809 Adam, J., Oberti, R., Camara, F., Green, T.H., 2007. An Electron microprobe, LAM-
810 ICP-MS and single-crystal X-ray structure refinement study of the effects of
811 pressure, melt-H2O concen- tration and fO2 on experimentally produced basaltic
812 amphiboles. European Journal of Mineralogy 19 (5), 641-655. DOI:
813 10.1127/0935-1221/2007/0019-1750

814 Anderson, J.L., Smith, D.R., 1995. The effects of temperature and fO_2 in the Al-in-
815 hornblende barometer. American Mineralogist 80, 549-559. DOI: 10.2138/am-
816 1995-5-614.

817 Arculus, R.J., 2003. Use and Abuse of the Terms Calcalkaline and Calcalkalic. Journal
818 of Petrology 44, 929-935. DOI:10.1093/petrology/44.5.929.

819 Bacon, C.R., Druitt, T.H., 1988. Compositional Evolution of the Zoned Calcalkaline
820 Magma Chamber of Mount-Mazama, Crater Lake, Oregon. Contributions to
821 Mineralogy and Petrology 98 (2), 224-256.

822 Barclay, J., Carmichael, I.S.E., 2004. A hornblende basalt from western Mexico: water-
823 saturated phase relations constrain a pressure-temperature window of
824 eruptibility. Journal of Petrology 45, 485-506. DOI: 10.1093/petrology/egg091

825 Bea, F., 1996. Residence of REE, Y, Th and U in Granites and Grustal Protoliths;
826 Implications for the Chemistry of Crustal Melts. Journal of Petrology 37 (3),
827 521-552. DOI: 10.1093/petrology/37.3.521.

828 Bea, F., Montero, P., Ortega, M., 2006. A LA-ICP-MS evaluation of Zr reservoirs in
829 common crustal rocks: implications for Zr and Hf geochemistry, and zircon-
830 forming processes. The Canadian Mineralogist 44, 693-714.

831 Behrens, H., Gaillard, F., 2006. Geochemical Aspects of Melts: Volatiles and Redox
832 Behavior: Elements 2, 275-290. DOI: 10.2113/gselements.2.5.275.

833 Benedini, L., Gregori, D., 2013. Significance of the Early Jurassic Garamilla formation
834 in the western Nordpatagonian Massif. Journal of South American Earth
835 Sciences 45, 259-277. DOI: 10.1016/j.jsames.2013.03.016

836 Blundy, J., Cashman, K., 2008. Petrologic Reconstruction of Magmatic System
837 Variables and Processes. Reviews in Mineralogy and Geochemistry 69 (1): 179-
838 239. http://sci-hub.tw/https://doi.org/10.2138/rmg.2008.69.6

839 Blundy, J., Cashman K., Humphreys, M., 2006. Magma heating by decompression-
840 driven crystallization beneath andesite volcanoes. Nature 443, 76-80. DOI:
841 10.1038/nature05100.

842 Boehnke, P., Watson, E.B., Trail, D., Harrison, T.M., Schmitt, A.K., 2013. Zircon
843 saturation re-revisited. Chemical Geology 351, 324,334. DOI:
844 10.1016/j.chemgeo.2013.05.028.

845 Bouhier, V.E., Franchini, M.B., Caffe, P.J., Maydagán, L., Rapela, C.W., Paolini, M.,
846 2017. Petrogenesis of volcanic rocks that host the world-class Ag-Pb Navidad
847 District, North Patagonian Massif: Comparison with the Jurassic Chon Aike
848 Volcanic Province of Patagonia, Argentina. Journal of Volcanology and
849 Geothermal Research 338, 101-120. DOI: 10.1016/j.jvolgeores.2017.03.016.

850 Buddington, A.F., Lindsley, D.H., 1964. Iron-titanium oxide minerals and synthetic
851 equivalents. Journal of Petrology 5(2), 310-357. DOI: 10.1093/petrology/5.2.310

852 Cashman,, K.V, Sparks, R.S.J., Blundy, J.D., 2017. Vertically extensive and unstable
853 magmatic systems: A unified view of igneous processes. Science 355(6331),
854 eaag3055. DOI: 10.1126/science.aag3055.

855 Cortiñas, J.S., 1996. La cuenca de Somuncurá-Cañadón Asfalto: sus límites, ciclos
856 evolutivos del relleno sedimentario y posibilidades exploratorias. XIII Congreso
857 Geológico Argentino and III Congreso de Exploración de Hidrocarburos,
858 Buenos Aires, Argentina, pp. 147-163.

859 Cúneo, R., Ramezani, J., Scasso, R., Pol, D., Escapa, I., Zavattieri, A.M., Bowring,
860 S.A., 2013. High-precision U-Pb geochronology and a new chronostratigraphy
861 for the Cañadón Asfalto Basin, Chubut, central Patagonia: Implications for
862 terrestrial faunal and floral evolution in Jurassic. Gondwana Research 24, 1267-
863 1275. DOI: 10.1016/j.gr.2013.01.010.

864 Dale, J., Powell, R., White, R.W., Elmer, F.L., Holland, T.J.B., 2005. A thermodynamic
865 model for Ca-Na clinoamphiboles in Na2O-CaO-FeO-MgO-Al2O3-SiO2-H2O-
866 O for petrological calculations. Journal of Metamorphic Geology 23, 771-791.
867 DOI:10.1111/j.1525-1314.2005.00609.x

868 Davidson, J., Turner, S., Plank, T., 2013. Dy/Dy*: Variations arising from mantle
869 sources and petrogenetic processes. Journal of Petrology 54, 525-537. DOI:
870 10.1093/petrology/egs076.

871 Demény, A., Harangi, S., Vennemann, T.W., Casillas, R., Horváth, P., Milton, A.J.,
872 Mason, P.R.D., Ulianov, A., 2012. Amphiboles as indicators of mantle source
873 contamination: Combined evaluation of stable H and O isotope compositions
874 and trace element ratios. Lithos 152, 141-156. DOI:10.1016/j.lithos.2012.07.001

875 Dejonghe, L., Darras, B., Hughes, G., Muchez, P., Scoates, J., Weis, D., 2002. Isotopic
876 and fluid-inclusion constraints on the formation of polymetallic vein deposits in
877 the central Argentinian Patagonia. Mineralium Deposita 37 (2), 158-172. DOI:
878 10.1007/s00126-001-0225-8.

879 Echaurren, A., Folguera, A., Gianni, G., Orts, D., Tassara, A., Encinas, A., Giménez,
880 M., Valencia, V., 2016. Tectonic evolution of the North Patagonian Andes (41°-
881 44° S) through recognition of syntectonic strata. Tectonophysics 677, 99-114.
882 DOI: 10.1016/j.tecto.2016.04.009.

883 Echaurren, A., Oliveros, V., Folguera, A., Ibarra, F., Creixell, C., Lucassen, F., 2017.
884 Early Andean tectonomagmatic stages in north Patagonia: insights from field
885 and geochemical data. Journal of the Geological Society 174 (3), 405-421. DOI:
886 10.1144/jgs2016-087.

887 Féraud, G., Alric, V., Fornari, M., Bertrand, H., Haller, M., 1999. 40Ar -39Ar dating or
888 the Jurassic volcanic province of Patagonia: migrating magmatism related to
889 Gondwana break-up and subduction. Earth and Planetary Science Letters 172,
890 83-96. DOI: 10.1016/S0012-821X(99)00190-9.

891 Figari, E.G., Courtade, S.F., 1993. Evolución tectosedimentaria de la Cuenca de
892 Cañadón Asfalto, Chubut, Argentina. XII Congreso Geológico Argentino and II
893 Congreso de Exploración de Hidrocarburos, pp. 66-77.

894 Figari, E.G., Scasso, R.A., Cúneo, R.N., Escapa, I., 2015. Estratigrafía y evolución
895 geológica de la Cuenca de Cañadón Asfalto, Provincia del Chubut, Argentina.
896 Latin American Journal of Sedimentology and Basin Analysis 22 (2): 135-169.

897 Franzese, J.R., Pankhurst, R.J., Rapela, C.W., Spalletti, L.A., Fanning, C.M.,
898 Muravchick, M., 2002. Nuevas evidencias geocronológicas sobre el

magmatismo gondwánico en el noroeste del Macizo Norpatagónico. In: C.N. Cingolani, C.A., Linares, E., López de Luchi, M.G., Ostera, H.A., Panarello, H. O. (Eds.), Actas del XV Congreso Geológico Argentino, El Calafate/Santa Cruz, Argentina, pp. 144-148.

Gill, J.B., 1981. Orogenic Andesite and Plate Tectonics. Springer Verlag, New York.

Gordon, A., Ort, M.H., 1993. Edad y correlación del plutonismo subcordillerano de las provincias de Río Negro y Chubut (41º-42º30'L.S.). In XII Congreso Geológico Argentino and II Congreso de Exploración de Hidrocarburos, Actas 4, 120-127.

Grove, T.L., Elkins-Tanton, L.T., Parman, S.W., Chatterjee, N., Müntener, O., Gaetani, G.A., 2003. Fractional crystallization and mantle-melting controls on calc-alkaline differentiation trends. Contributions to Mineralogy and Petrology 145, 515-533. DOI: 10.1007/s00410-003-0448-z

Gust, D.A., Biddle, K.T., Phelps, D.W., Uliana, M.A., 1985. Associated Middle to Late Jurassic volcanism and extension in Southern South America. Tectonophysics 116, 223-253. DOI: 10.1016/0040-1951(85)90210-0

Haggerty, S., 1991. Oxide textures; a mini-atlas. In: Lindsley, D.H. (Ed.), Oxide Minerals: Petrologic and Magnetic Significance. Reviews in Mineralogy and Geochemistry 25. Mineralogist Society of America, Washington D.C., pp. 129-219.

Haller, M.J., Linares, E., Ostera, H., Page, S., 1999. Petrology and geochronology of the Sub-Cordilleran Plutonic Belt of Patagonia. In: II South American Symposium on Isotope Geology, Carlos Paz, Argentina, Segemar, Buenos Aires, pp. 210-214.

922 Hammarstrom J.M. and Zen E., 1986. Aluminum in hornblende: an empirical igneous
923 geobarometer. American Mineralogist 71: 1297–1313.

924 Harrison, T.M., Watson, E.B., 1983. Kinetics of zircon dissolution and zirconium
925 diffusion in granitic melts of variable water content. Contributions to
926 Mineralogy and Petrology 84, 66-72.

927 Harrison, T.M., Watson, E.B., 1984. The behavior of apatite during crustal anatexis:
928 equilibrium and kinetic considerations. Geochimica et Cosmochimica Acta 48,
929 1467-1477.

930 Hauser, N., Cabaleri, N.G., Gallego, O.F., Monferran, M.D., Silva Nieto, D., Armella,
931 C., Matteini, M., Aparicio González, P.A., Pimentel, M.M., Volkheimer, W.,
932 Reimold, W.U., 2017. U-Pb and Lu-Hf zircon geochronology of the Cañadón
933 Asfalto Basin, Chubut, Argentina: Implications for the magmatic evolution in
934 central Patagonia. Journal of South American Earth Sciences 78, 190-212. DOI:
935 10.1016/j.jsames.2017.05.001.

936 Holland, T., Blundy, J., 1994. Non-ideal interactions in calcic amphiboles and their
937 bearing on amphibole-plagioclase thermometry. Contributions to Mineralogy
938 and Petrology 116, 433-447. DOI: 10.1007/BF00310910.

939 Hollister L.S., Grissom G.C., Peters E.K., Stowell H.H., Sisson V.B., 1987.
940 Confirmation of the empirical correlation of Al in hornblende with pressure of
941 solidification of calc-alkaline plutons. American Mineralogist 72: 231–239.

942 Hora, J.M., Singer, B.S., Wörner, G., Beard, B.L., Jicha, B.R., Johnson, C.M., 2009.
943 Shallow and deep crustal control on differentiation of calc-alkaline and tholeiitic
944 magma. Earth and Planetary Science Letters 285, 75-86.
945 DOI:10.1016/j.epsl.2009.05.042

946 Irvine, T.N., Baragar, W.R.A., 1971. A guide to the chemical classification of the
947 common volcanic rocks. Canadian Journal of Earth Sciences 8, 523-548.

948 Johnson M.C. and Rutherford M.J., 1989. Experimental calibration of the aluminum-in-
949 hornblende geobarometer with application to Long Valley caldera (California)
950 volcanic rocks. Geology 17 (9): 837-841. DOI:10.1130/0091-
951 7613(1989)017<0837.

952 Kay, S.M., Burns, W.M., Copeland, P., 2006. Upper Cretaceous to Holocene
953 magmatism and evidence for transient Miocene shallowing of the Andean
954 subduction zone under the northern Neuquén Basin: Geological Society of
955 America, Special Paper, pp. 19-60. DOI: 10.1130/2006.2407(02).

956 Kiss, B., Harangi, S., Ntaflos, T., Mason, P.R.D., Pál-Molnár, E., 2014. Amphibole
957 perspective to unravel pre-eruptive processes and conditions in volcanic
958 plumbing systems beneath intermediate arc volcanoes: A case study from
959 Ciomadul volcano (SE Carpathians). Contributions to Mineralogy and Petrology
960 167, 1-27. DOI: 10.1007/s00410-014-0986-6.

961 Krawczynski, M., Grove, T., Behrens, H., 2012. Amphibole stability in primitive arc
962 magmas: effects of temperature, H2O content, and oxygen fugacity.
963 Contributions to Mineralogy and Petrology 164 (2), 317-339. DOI:
964 10.1007/s00410-012-0740-x

965 Leake, B.E., Wooley, A.R., Arps, C.E.S., Birch, W.D., Gilbert, M.C., Grice, J.D.,
966 Hawthorne, F.C., 1997. Nomenclature of amphiboles: report of the
967 subcommittee on amphiboles of the International Mineralogical Association
968 Commission on new minerals and mineral names. Canadian Mineralogist 35,
969 1571-1606. DOI:10.1180/minmag.1997.061.405.13

970 Le Bas, M.J., 1962. The role of aluminium in igneous clinopyroxenes with relation to
971 their parentage. American Journal of Sciences 260, 267-288.

972 Leterrier, J., Maury, R.C., Thonon, P., Girard, D., Marchal, M., 1982. Clinopyroxene
973 composition as a method of identification of the magmatic affinities of
974 paleovolcanic series. Earth and Planetary Science Letters 59, 139-154. DOI:
975 10.1016/0012-821X(82)90122-4

976 López de Luchi, M.G., Cerredo, M.E., 2008. Geochemistry of the Mamil Choique
977 granitoids at Rio Chico, Río Negro, Argentina: Late Paleozoic crustal melting in
978 the North Patagonian Massif. Journal of South American Earth Sciences 25 (4),
979 526-546. DOI: 10.1016/j.jsames.2007.05.004.

980 Matsui, Y., Onuma, N., Nagasawa, H., Higuchi, H., Banno, S., 1977. Crystal structure
981 control in trace element partition between crystal and magma. Tectonics 100,
982 315-324.

983 McDonough, W.F., Sun, S.–s., 1995. The composition of the Earth. Chemical Geology
984 120, 223-253. DOI: 10.1016/0009-2541(94)00140-4

985 Miyashiro, A., 1974. Volcanic rock series in island arcs and active continental margins.
986 American Journal of Sciences 274, 321-355. DOI:10.2475/ajs.274.4.321

987 Molina, J.F., Scarrow, J.H., Montero, P.G., Bea, F., 2009. High-Ti amphibole as a
988 petrogenetic indicator of magma chemistry: Evidence for mildly alkalic-hybrid
989 melts during evolution of Variscan basic-ultrabasic magmatism of Central
990 Iberia. Contributions to Mineralogy and Petrology 158, 69-98.
991 DOI:10.1007/s00410-008-0371-4

992 Molina, J.F., Montero, P., Bea, F., Scarrow, J.H., 2012. Anomalous xenocryst
993 dispersion during tonalite–granodiorite crystalmush hybridization in the mid
994 crust: mineralogical and geochemical evidence from Variscan appinites (Ávila
995 Batholith, Central Iberia). Lithos 153, 224-242.

996 Molina, J.F., Moreno, J.A., Castro, A., Rodríguez, C., Fershtater, G.B., 2015. Calcic
997 amphibole thermobarometry in metamorphic and igneous rocks: New
998 calibrations based on plagioclase/amphibole Al-Si partitioning and
999 amphibole/liquid Mg partitioning. Lithos 232, 286-305. DOI:
1000 10.1016/j.lithos.2015.06.027.

1001 Moreno, J.A., Molina, J.F., Bea, F., Anbar, M.A., Montero, P., 2016. Th-REE- and Nb-
1002 Ta-accessory minerals in post-collisional Ediacaran felsic rocks from the
1003 Katerina Ring Complex (S. Sinai, Egypt): an assessment for the fractionation of
1004 Y/Nb, Th/Nb, La/Nb and Ce/Pb in highly evolved A-type granites. Lithos 258-
1005 259, 173-196. DOI: 10.1016/j.lithos.2016.04.020.

1006 Moreno, J.A., Molina, J.F., Montero, P., Anbar, M.A., Scarrow, J.H., Cambeses, A.,
1007 Bea, F., 2014. Unraveling sources of A-type magmas in juvenile continental
1008 crust: constraints from compositionally diverse Ediacaran post-collisional
1009 granitoids in the Katerina Ring Complex, southern Sinai, Egypt. Lithos 192-195,
1010 56-85. DOI: 10.1016/j.lithos.2014.01.010.

1011 Morimoto, N., 1988. Nomenclature of Pyroxenes. Mineralogy and Petrology 39 (1), 55-
1012 76. DOI: 10.1007/BF01226262.

1013 Munker, C., Wörner, G., Yogodzinski, G., Churikova, T., 2004. Behaviour of high field
1014 strength elements in subduction zones: Constraints from Kamchatka-Aleutian

1015 arc lavas. Earth and Planetary Science Letters 224, 275-293. DOI:
1016 10.1016/j.epsl.2004.05.030.

1017 Nagasawa, H., Schnetzler, C.C., 1971. Partitioning of rare Earth, alkali, and alkaline
1018 Earth elements between phenocrysts and acidic igneous magmas. Geochimica et
1019 Cosmochimica Acta 35, 953-968. DOI: 10.1016/0016-7037(71)90008-1.

1020 Nisbet, E.G., Pearce, J.A., 1977. Clinopyroxene composition in mafic lavas from
1021 different tectonic settings. Contributions to Mineralogy and Petrology 63, 149-
1022 160. DOI:10.1007/BF00398776

1023 Nullo, F., Proserpio, C., 1975. La Formación Taquetrén en Cañadón del Zaino (Chubut)
1024 y sus relaciones estratigráficas en el ámbito de la Patagonia, de acuerdo a la
1025 flora, República Argentina. Revista de la Asociación Geológica Argentina 30,
1026 133-150.

1027 Nullo, F.E., 1978. Descripción Geológica de la Hoja 41d, Lipetrén, Provincia de Río
1028 Negro (1:200000), edited, pp. 1-88, Secretaría del Estado de Minería, Ministerio
1029 de Economía, República Argentina, Boletín Nº 158.

1030 O´Neill, H.S., Pownceby M.I., 1993. Thermodynamic data from redox reactions at high
1031 temperatures. I. An experimental and theoretical assessment of the
1032 electrochemical method using stabilized zirconia electrolytes, with revised
1033 values for the Fe-“FeO”, Co-CoO, Ni-NiO and Cu-Cu2O oxygen buffer.
1034 Contributions to Mineralogy and Petrology 14, 296-314. DOI:
1035 10.1007/BF01046533.

1036 Page, S., 1984. Los gabros bandeados de la Sierra de Tepuel: cuerpos del sector sudeste.
1037 In Actas 9º Congreso Geológico Argentino, pp. 584-599, Bariloche.

1038 Page, R., Page, S., 1993. Petrología y significado tectónico del Jurásico volcánico de
1039 Chubut central. Revista de la Asociación Geológica Argentina 1, 174-176.

1040 Page, S., Page, R., 1999. Las diabasas y gabros del Jurásico de la Precordillera del
1041 Chubut. In: Caminos, R. (Ed.). Geologia Argentina. Subsecretaria de Mineria de
1042 la Nación, Servicio Geológico Minero Argentina, Instituto de Geología y
1043 Recursos Minerales 29, 489-495.

1044 Pankhurst, R.J., Rapela, C.W., 1995. Production of Jurassic rhyolite by anatexis of the
1045 lower crust of Patagonia. Earth and Planetary Science Letters 134, 23-26. DOI:
1046 10.1016/0012-821X(95)00103-J

1047 Pankhurst, R.J., Sruoga, P., Rapela, C., 1993. Estudio geocronológico Rb/Sr de los
1048 Complejos Chon Aike y El Quemado a los 47º 30' LS. XII Congreso Geológico
1049 Argentino, Mendoza, pp. 171-178.

1050 Pankhurst, R.J., Rapela, C.W., Fanning, C.M., Márquez, M., 2006. Gondwanide
1051 continental collision and the origin of Patagonia. Earth Science Reviews 76,
1052 235-257. DOI: 10.1016/j.earscirev.2006.02.001

1053 Pankhurst, R.J., Riley, T.R., Fanning, C.M., Kelley, S.P., 2000. Episodic silicic
1054 volcanism in Patagonia and the Antarctic Peninsula: chronology of magmatism
1055 associated with the break-up of Gondwana. Journal of Petrology 41, 605-625.
1056 DOI: 10.1093/petrology/41.5.605

1057 Pankhurst, R.J., Leat, P.T., Sruoga, P., Rapela, C.W., Márquez, M., Storey, B.C., Riley,
1058 T.R., 1998. The Chon Aike province of Patagonia and related rocks in West
1059 Antarctica: A silicic large igneous province. Journal of Volcanology and
1060 Geothermal Research 81, 113-136. DOI: 10.1016/S0377-0273(97)00070-X

1061 Parat, F., Dungan, M.A., Lipman, P.W., 2018. Contemporaneous Trachyandesitic and
1062 Calc-alkaline Volcanism of the Huerto Andesite, San Juan Volcanic Field,
1063 Colorado, USA. Journal of Petrology 46(5), 859–891.
1064 https://doi.org/10.1093/petrology/egi003

1065 Peccerillo, A., Taylor, S.R., 1976. Geochemistry of Eocene calcalkaline volcanic rocks
1066 from the Kastamonu Area, Northern Turkey. Contributions to Mineralogy and
1067 Petrology 58, 63-81. DOI: 10.1007/BF00384745

1068 Pichavan, M., Martel, C., Bourdier, J.L., Scaillet, B., 2002. Physical conditions,
1069 structure, and dynamics of a zoned magma chamber: mount Peleé (Martinique,
1070 Lesser Antilles Arc). Journal of Geophysical Research 107 (B5), ECV 1-1-ETG
1071 5-16.. DOI:10.1029/2001JB000315

1072 Poma, S., 1986. Petrología de las rocas básicas precretácicas de la sierra de Tepuel,
1073 provincia del Chubut. Ph.D. thesis, 256 pp, Universidad de Buenos Aires,
1074 Buenos Aires.

1075 Proserpio, C.A., 1978. Descripción Geológica de la Hoja 42d, Gastre, Provincia del
1076 Chubut (1:200000), edited, pp. 1-75, Secretaría del Estado de Minería,
1077 Ministerio de Economía, Boletín Nº 159.

1078 Putirka, K.D., 2008. Thermometers and barometers for volcanic systems. Minerals,
1079 Inclusions and Volcanic Processes. Reviews in Mineralogy and Geochemistry
1080 69, 61-120. DOI: 10.2138/rmg.2008.69.3

1081 Putirka, K., 2016. Amphibole thermometers and barometers for igneous systems, and
1082 some implications for eruption mechanisms of felsic magmas at arc volcanoes.
1083 American Mineralogist 101, 841-858. DOI:10.2138/am-2016-5506

1084 Ramos, V.A, Cristallini, E., & Introcaso, A., 2004. The Andean Thrust System—
1085 Latitudinal Variations in Structural Styles and Orogenic Shortening. Aapg
1086 Memoir, 82, 30–50.

1087 Rapela, C.W., Pankhurst, R.J., 1992. The granites of northern Patagonia and the Gastre
1088 Fault System in relation to the break-up of Gondwana. In: A.T. Storey, B.C.,
1089 Pankhurst, R.J. (Eds.), Magmatism and the Causes of Continental Break-Up,
1090 Geological Society of London Special Publication, pp. 209-220. DOI:
1091 10.1144/GSL.SP.1992.068.01.13

1092 Rapela, C.W., Pankhurst, R.J., Fanning, C.M., Hervé, F., 2005. Pacific subduction
1093 coeval with the Karoo mantle plume: the Early Jurasssic Subcordilleran belt of
1094 northwestern Patagonia. Geological Society, London, Special Publications 246,
1095 217-239. DOI: 10.1144/GSL.SP.2005.246.01.07

1096 Rapela, C.W., Dias, G.F., Franzese, J.R., Alonso, G., Benvenuto, A.R., 1991. El
1097 Batolito de la Patagonia central: evidencias de un magmatismo triásico-jurásico
1098 asociado a fallas transcurrentes. Revista Geológica de Chile 18 (2), 121-138.

1099 Reguzzoni, M., Sampietro, D., 2015. GEMMA: An Earth crustal model based on
1100 GOCE satellite data. International Journal of Applied Earth Observation and
1101 Geoinformation 35 (PA), 31-43DOI: 10.1016/j.jag.2014.04.002

1102 Ridolfi, F., Renzulli, A., 2012. Calcic amphiboles in calc-alkaline and alkaline magmas:
1103 thermobarometric and chemometric empirical equations valid up to 1130 °C and
1104 2.2 GPa. Contributions to Mineralogy and Petrology 163 (5), 877-895. DOI:
1105 10.1007/s00410-011-0704-6

1106 Ridolfi, F., Renzulli, A., Puerini, M., 2010. Stability and chemical equilibrium of
1107 amphibole in calc-alkaline magmas: An overview, new thermobarometric

formulations and application to subduction-related volcanoes. Contributions to Mineralogy and Petrology 160, 45-66. DOI:10.1007/s00410-009-0465-7

Ridolfi, F., Puerini, M., Renzulli, A., Menna, M., Toulkeridis, T., 2008. The magmatic feeding system of El Reventador volcano (Sub-Andean zone, Ecuador) constrained by texture, mineralogy and thermobarometry of the 2002 erupted products. Journal of Volcanology and Geothermal Research 176, 94-106. DOI: 10.1016/j.jvolgeores.2008.03.003

Riley, T.R., Leat, P., Pankhurst, R.J., Harris, C., 2001. Origins of Large Volume Rhyolitic Volcanism in the Antarctic Peninsula and Patagonia by Crustal Melting. Journal of Petrology 42 (6), 1043-1065. DOI: 10.1093/petrology/42.6.1043

Rudnick, R.L., Gao, L., 2003. Composition of the continental crust. In: Rudnick, R.L. (Ed.) Treatise on Geochemistry. Elsevier, 1-64.

Rutherford, M.J., Devine, J.D., 2008. Magmatic conditions and processes in the storage zone of the 2004-2006 Mount St. Helens Dacite. In: Sherrod, D.R., Scott, W.E., Stauffer, PH. (Eds.) A Volcano Rekindled: the renewed eruption of Mount St. Helens, 2004-2006. US Geol Surv Prof Paper 1750, Chapter 31, pp. 703-725.

Sas, M., Debari, S.M., Clynne, M.A., Rusk, B.G., 2017. Using mineral geochemistry to decipher slab, mantle, and crustal input in the generation of high-Mg andesites and basaltic andesites from the northern Cascade Arc. American Mineralogist 102, 948- LP-965. DOI: 10.2138/am-2017-5756.

Sato, A.M., Basei, M.A.S., Tickyj, H., Llambías, E.J., Varela, R., 2004. Granodiorita El Sótano: Plutón jurásico deformado aflorante en el basamento de Las Grutas,

1131 Macizo Norpatagónico Atlántico. Revista de la Asociacion Geologica Argentina
1132 59, 591-600.

1133 Scarrow, J.H., Molina, J.F., Bea, F., Montero, P., 2009. Within-plate calc-alkaline
1134 rocks: insights from alkaline mafic magma-peraluminous crustal melt hybrid
1135 appinites of the Central Iberian Variscan continental collision. Lithos 110, 50-
1136 64. DOI: 10.1016/j.lithos.2008.12.007

1137 Schmidt, M.W., 1992. Amphibole composition in tonalite as a function of pressure : an
1138 experimental calibration of the Al-in-hornblende barometer. Contributions to
1139 Mineralogy and Petrology 110: 304–310. DOI: 10.1007/BF00310745

1140 Schnetzler, C.C., Philpotts, J.A., 1970. Partition coefficients of rare-earth elements
1141 between igneous matrix material and rock-forming mineral phenocrysts; II.
1142 Geochimica et Cosmochimica Acta 34 (3), 331-340. doi: 10.1016/0016-
1143 7037(70)90110-9

1144 Simakin, A., Zakrevskaya, O., Salova, T., 2012. Novel Amphibole Geobarometer with
1145 application to mafic xenoliths. Earth Science Research 1 (2), 82-97. DOI:
1146 10.5539/esr.v1n2p82

1147 Sisson, T.W., 1994. Hornblende-melt trace-element partitioning measured by ion
1148 microprobe. Chemical Geology 117, 331-344. DOI: 10.1016/0009-
1149 2541(94)90135-X

1150 Sisson, T.W., Grove, T.L., 1993. Experimental investigations of the role of H2O in
1151 calc-alkaline differentiation and subduction zone magmatism. Contributions to
1152 Mineralogy and Petrology 113, 143-166. DOI:10.1007/ BF00283225

1153 Suárez, M., Márquez, M., 2007. A Toarcian retro-arc basin of Central Patagonia
1154 (Chubut), Argentina: Middle Jurassic closure, arc migration and tectonic setting:
1155 Andean Geology 34, 63-79.

1156 Sun, S.–s., McDonough, W.F., 1989. Chemical and isotopic systematics of oceanic
1157 basalts: implications for mantle composition and processes. Geological Society
1158 of London, Special Publication 42, 313-345. DOI:
1159 10.1144/GSL.SP.1989.042.01.19

1160 Tiepolo, M., Oberti, R., Zanetti, A., Vannucci, R., Foley, S.F., 2007. Trace element
1161 partitioning between amphibole and silicate melt. In: Hawthorne, F.C., Oberti,
1162 R., Della Ventura, G., Mottana, A. (Eds.) Amphiboles. Crystal chemistry,
1163 occurrence and health issues. Reviews in Mineralogy and Geochemistry 67.
1164 Mineralogical Society of America and Geochemical Society, Chantilly, pp 417-
1165 452. DOI: 10.2138/rmg.2007.67.11

1166 Vizán, H., 1998. Paleomagnetism of the Lower Jurassic Lepá and Osta Arena for-
1167 mations, Argentine Patagonia. Journal of South American Earth Sciences 11,
1168 333-350. DOI: 10.1016/S0895-9811(98)00018-2

1169 Volkheimer, W., 1964. Estratigrafía de la región extra-andina del Departamento de
1170 Cushamen (Chubut), entre los paralelos 42º y 42º 30´ y los meridianos 70º y 71º.
1171 Revista de la Asociación Geológica Argentina 20 (2), 85-107.

1172 Whitney, D.L., Evans, B.W., 2010. Abbreviations for names of rock-forming minerals.
1173 American Mineralogist 95, 185-187. DOI: 10.2138/am.2010.3371

1174 Winchester, J.A., Floyd, P.A., 1977. Geochemical discrimination of different magma
1175 series and their differentiation products using inmobile elements. Chemical
1176 Geology 20, 325-343. DOI: 10.1016/0009-2541(77)90057-2

1177 Wörner, G., Harmon, R.S., Davidson, J., Moorbath, S., Turner, D.L., Mcmillan, N.,
1178 Nye, C., López-Escobar, L., Moreno, H., 1988. The Nevados de Payachata
1179 volcanic region (18°S/69°W, N. Chile). Bulletin of Volcanology 50, 287-303.
1180 DOI: 10.1007/BF01073587

1181 Zaffarana, C.B., Somoza, R., 2012. Palaeomagnetism and 40Ar/39Ar dating from
1182 Lower Jurassic rocks in Gastre, central Patagonia: further data to explore
1183 tectonomagmatic events associated with the break-up of Gondwana. Journal of
1184 the Geological Society 169 (4), 371-379. DOI: 10.1144/0016-76492011-089

1185 Zaffarana, C. B., Somoza, R., López de Luchi, M., 2014. The Late Triassic Central
1186 Patagonian Batholith: Magma hybridization, $^{40}Ar/^{39}Ar$ ages and
1187 thermobarometry. Journal of South American Earth Sciences, 55, 94–122.
1188 https://doi.org/10.1016/j.jsames.2014.06.006

1189 Zaffarana, C. B., Somoza R., Orts, D.L., Mercader, R., Boltshauser, B., Ruiz González,
1190 V., Puigdomenech, C., 2017. Internal structure of the Central Patagonian
1191 Batholith at Gastre. GEOSPHERE 13 (6), 1973-1992. DOI:
1192 10.1130/GES01493.1

1193 Zaffarana, C. B., Lagorio, S., Orts, D., Busteros, A., Silva Nieto, D., Giacosa, R., Ruiz
1194 González, V., Boltshauser, B., Puigdomenech Negre, C., Somoza, R., Haller,
1195 M., 2018. First geochemical and geochronological characterization of Late
1196 Cretaceous mesosilicic magmatism in Gastre, Northern Patagonia, and its
1197 tectonic relation to other coeval volcanic rocks in the region. Geological
1198 Magazine 1-10. DOI: 10.1017/S0016756818000432

1199 Zhang, J., Humphreys, M., Cooper, G.F., Davidson, D.P., Macpherson, C.G., 2017.
1200 Magma mush chemistry at subduction zones, revealed by new melt major

element inversion from calcic amphiboles. American Mineralogist 102, 1353-1367. DOI: http://dx.doi.org/10.2138/am-2017-5928

outcrop	T0	T1	G2-63	G3-134	G3-157
	andesitic lava	andesitic lava	andesitic porphyry	andesitic dike	andesitic lava
Main rock type	Amp-dacite	Amp-trachydacite	Amp-dacite	Amp-andesite	Cpx-trachydacite
Phenocrysts and microphenocrysts	Pl + Amp	Pl+Amp+Cpx+Bt	Pl+Amp+Bt	Pl+Amp (Cpx cores in Amp)	Pl+Cpx (Amp microphenocrysts)
Accesory minerals	Titanomagnetite, apatite, titanite				
SiO_2	63.17	61.60	61.79	58.57	59.72
TiO_2	0.53	0.56	0.56	0.96	1.46
Al2O3	16.85	17.33	17.83	16.12	15.56
FeO_t	5.31	4.98	4.80	6.50	6.78
MnO	0.08	0.09	0.09	0.07	0.17
MgO	2.51	3.78	3.50	4.97	3.04
CaO	4.97	4.16	4.96	6.29	5.93
Na_2O	4.60	5.22	4.68	3.86	5.27
K_2O	1.83	2.10	1.61	2.31	1.47
P_2O_5	0.14	0.17	0.19	0.35	0.59
LOI	1.99	2.31	2.20	1.90	2.10
Total	100.00	100.00	100.00	100.00	100.00
U	1.10	0.70	0.42	1.30	0.77
Th	3.80	2.50	1.90	4.00	4.40
Zr	115.00	111.00	128.00	292.00	266.00
Hf	2.70	2.90	5.10	12.40	12.40
Ta	0.60	0.50	0.40	1.80	0.60
Nb	5.00	4.00	4.00	7.00	6.00
Y	10.00	10.00	9.10	14.70	25.10
Ba	766.00	1253.00	982.00	1000.00	970.00
Sr	658.00	602.00	721.40	771.10	594.80
Cs	<0.5	3.40			
Rb	37.00	38.00	34.40	78.90	29.20
Cr	100.00	110.00	61.00	84.00	8.00
Ni	30.00	30.00	26.00	80.00	5.00
La	20.70	18.10	16.00	30.40	26.20
Ce	40.20	38.20	30.80	85.10	78.50
Pr	4.38	4.50	3.45	9.72	9.14
Nd	16.10	17.80	12.70	32.30	30.40
Sm	3.20	3.60	2.30	7.40	7.40
Eu	0.93	1.00	0.77	1.91	2.04
Gd	2.70	3.10	2.05	5.68	6.91
Tb	0.40	0.40	0.33	0.79	0.93
Dy	2.10	2.40	1.75	3.91	5.57
Ho	0.40	0.40	0.33	0.66	1.08
Er	1.20	1.30	0.81	1.65	2.85
Tm	0.17	0.18	0.13	0.27	0.39
Yb	1.10	1.10	0.90	1.50	2.40
Lu	0.18	0.19	0.15	0.23	0.39
Pb	18.00	10.00	9.00	19.00	48.00
Ga	19.00	20.00	19.00	20.00	19.00

outcrop	T0	T1	G2-63	G3-134	G3-157
	andesitic lava	andesitic lava	andesitic porphyry	andesitic dike	andesitic lava
Mg#	45.71	57.51	56.51	57.66	44.46
CA/Thindex	1.50	2.23	2.16	1.88	1.19
$[La/Yb]_N$	12.78	11.18	12.08	13.77	7.42
$[La/Sm]_N$	4.04	3.14	4.34	2.57	2.21
$[La/Dy]_N$	10.23	7.83	9.49	8.07	4.88
$[Ho/Lu]_N$	1.00	0.95	0.99	1.29	1.25
$[Dy/Yb]_N$	1.25	1.43	1.27	1.71	1.52
La/Sm	6.47	5.03	6.96	4.11	3.54
Sm/Yb	2.91	3.27	2.56	4.93	3.08
Eu/Eu*	0.96	0.91	1.08	0.90	0.87
Dy/Dy*	0.57	0.68	0.59	0.76	0.82
Dy/Yb	1.91	2.18	1.94	2.61	2.32
La/Ta	34.50	36.20	40.00	16.89	43.67
Ba/Nb	153.20	313.25	245.50	142.86	161.67
La/Nb	4.14	4.53	4.00	4.34	4.37
Nb/Zr	0.04	0.04	0.03	0.02	0.02
Nb/Ta	8.33	8.00	10.00	3.89	10.00
Ce/Pb	2.23	3.82	3.42	4.48	1.64
Th/Nb	0.76	0.63	0.48	0.57	0.73
Ba/La	18.21	17.21	19.21	21.21	22.21
Th/La	0.18	0.14	0.12	0.13	0.17
Ta/Hf	0.22	0.17	0.08	0.15	0.05
ASI index	0.91	0.94	0.97	0.79	0.74
Liquid-only-Molina et al. (2015)	992	1052	1032	1041	991
Liquid-only-Putirka (2016)-Eqn.3	960	1002	991	1008	1002
M value (Harrison & Watson 1983)	2.33	1.83	2.37	1.89	1.89
Zr-saturation T(ºC)-Harrison & Watson (1983)	740	644	730	722	725
Zr-saturation T(ºC)-Boehnke et al. (2013)	659	569	648	652	655
Ap-saturation T(ºC)-Harrison & Watson (1984)	910	877	1026	851	847

Mineral	**Amp**	**Amp**	**Amp**	**Amp**	**Amp**	**Amp**	**Amp**	**Amp**	**Amp**	**Amp**	**Amp**	**Amp**	**Amp**	**Amp**	**Amp**	**Amp**	**Amp**	**Amp**
Sample	**G2-63**	**G2-63**	**G2-63**	**G2-63**	**G2-63**	**G2-63**	**G2-63**	**G2-63**	**G2-63**	**G2-63**	**G2-63**	**G2-63**	**G2-63**	**G2-63**	**G2-63**	**G2-63**	**G2-63**	**G2-63**
Profile	**profile 1**	**profile 1**	**profile 1**	**profile 1**	**profile 1**	**profile 1**	**profile 1**	**profile 1**	**profile 1**	**profile 1**	**profile 2**	**profile 2**	**profile 2**	**profile 2**	**profile 2**	**profile 2**	**profile 3**	**profile 3**
Texture	**rim**	**rim**	**rim**	**center**	**center**	**center**	**rim**	**rim**	**rim**	**rim**	**rim**	**center**	**center**	**center**	**rim**	**rim**	**rim**	**rim**
Analysis	**1 / 1**	**2 / 1**	**3 / 1**	**4 / 1**	**5 / 1**	**6 / 1**	**7 / 1**	**8 / 1**	**9 / 1**	**10 / 1**	**16 / 1**	**17 / 1**	**18 / 1**	**19 / 1**	**20 / 1**	**21 / 1**	**63 / 1**	**64 / 1**
SiO_2	46.15	43.80	45.37	43.49	44.17	44.04	44.16	46.01	44.14	43.96	45.99	45.07	41.60	42.74	44.55	44.73	44.37	45.80
TiO_2	1.12	1.24	1.02	1.16	1.13	1.17	1.07	0.99	1.42	1.60	0.97	1.12	1.90	1.55	1.11	1.28	1.22	1.04
Al_2O_3	9.51	11.66	10.44	11.95	11.28	11.43	11.18	9.65	11.35	11.31	9.87	11.12	13.71	12.63	11.02	10.69	10.88	9.81
Cr_2O_3	0.00	0.00	0.01	0.01	0.01	0.02	0.02	0.00	0.00	0.00	0.00	0.02	0.02	0.03	0.00	0.03	0.04	0.00
NiO	0.04	0.00	0.02	0.03	0.01	0.02	0.00	0.03	0.02	0.00	0.03	0.05	0.00	0.06	0.00	0.02	0.03	0.09
FeO_t	13.82	14.99	14.45	15.44	15.17	14.90	14.87	14.30	14.64	14.33	14.54	14.33	14.95	14.94	14.88	14.53	14.71	14.91
MnO	0.39	0.33	0.40	0.37	0.35	0.31	0.41	0.37	0.34	0.41	0.41	0.33	0.25	0.31	0.33	0.38	0.38	0.42
MgO	14.37	12.93	14.01	12.68	13.27	13.35	13.27	13.97	13.14	13.42	13.69	12.88	11.55	12.03	12.95	13.19	13.05	13.53
CaO	10.59	10.33	10.54	10.67	10.67	10.52	10.42	10.48	10.36	10.44	10.57	10.70	10.98	10.95	10.44	10.30	10.33	10.29
Na_2O	1.66	1.96	1.68	1.90	1.87	1.89	1.85	1.71	1.95	1.91	1.68	1.73	2.13	2.02	1.81	1.80	1.89	1.65
K_2O	0.28	0.40	0.32	0.44	0.47	0.44	0.38	0.29	0.36	0.40	0.31	0.43	0.52	0.46	0.33	0.37	0.35	0.32
TOTAL	97.94	97.63	98.26	98.14	98.39	98.09	97.62	97.80	97.72	97.77	98.07	97.77	97.60	97.72	97.40	97.32	97.25	97.86
Geothermometers (ºC)																		
Ridolfi et al. (2010)-Eqn.1	848.64	-	-	-	-	-	-	846.54	-	-	849.27	-	-	-	-	-	-	844.78
Ridolfi & Renzulli (2012)-Eqn.2	869.28	-	-	-	-	-	-	863.16	-	-	864.29	-	-	-	-	-	-	870.35
Amph-only-Putirka (2016)-Eqn.5	829.88	864.90	838.59	-	-	-	854.01	825.04	865.91	873.65	823.84	-	-	-	844.93	846.73	851.62	820.34
Geobarometers (kbar)																		
Ridolfi et al. (2010)-Eqn.4	1.90	-	-	-	-	-	-	1.97	-	-	2.08	-	-	-	-	-	-	2.06
Ridolfi & Renzulli (2012)-Eqn.1d	-	-	-	-	-	-	-	-	-	-	-	-	-	-	-	-	-	-

Table 2a-Appendix

Mineral	**Amp**	**Amp**	**Amp**	**Amp**	**Amp**	**Amp**	**Amp**	**Amp**	**Amp**	**Amp**	**Amp**	**Amp**	**Amp**	**Amp**	**Amp**	**Amp**
Sample	**G2-63**	**G2-63**	**G2-63**	**G2-63**	**G2-63**	**G2-63**	**G2-63**	**G2-63**	**G2-63**	**G2-63**	**G3-157**	**G3-157**	**G3-157**	**G3-157**	**G3-157**	**G3-157**	**G3-157**
Profile	**profile 3**	**profile 3**	**profile 3**	**profile 4**	**profile 4**	**profile 4**	**profile 4**	**profile 4**	**profile 4**	**profile 4**	-	-	-	-	-	-	-
Texture	**center**	**center**	**center**	**rim**	**rim**	**rim**	**rim**	**center**	**center**	**center**	**center**	**center**	**rim**	**center**	**rim**	**center**	**rim**
Analysis	**65 / 1 .**	**66 / 1 .**	**67 / 1 .**	**70 / 1 .**	**71 / 1 .**	**72 / 1 .**	**73 / 1 .**	**74 / 1 .**	**75 / 1 .**	**76 / 1 .**	**32 / 1 .**	**73 / 1 .**	**74 / 1 .**	**75 / 1 .**	**76 / 1 .**	**77 / 1 .**	**78 / 1 .**
SiO_2	43.08	42.91	44.70	45.68	46.19	45.04	45.32	42.23	42.95	42.70	43.60	42.83	43.96	42.74	44.22	43.34	44.26
TiO_2	0.97	1.02	0.88	1.15	1.10	1.11	0.98	1.11	0.94	0.85	3.34	3.77	3.31	3.89	3.25	3.53	3.26
Al_2O_3	12.23	11.88	11.70	9.83	9.11	9.92	10.35	12.95	12.29	12.14	9.20	9.90	9.39	10.02	9.22	9.63	9.28
Cr_2O_3	0.05	0.01	0.00	0.03	0.04	0.00	0.02	0.00	0.02	0.00	0.01	0.06	0.00	0.00	0.00	0.02	0.00
NiO	0.05	0.00	0.03	0.00	0.00	0.00	0.00	0.03	0.00	0.00	0.00	0.00	0.00	0.01	0.02	0.00	0.00
FeO_t	15.79	16.07	15.54	13.97	13.96	14.64	14.68	16.44	15.87	16.26	11.34	11.61	11.76	11.62	11.35	11.80	11.43
MnO	0.43	0.38	0.44	0.36	0.36	0.40	0.33	0.43	0.45	0.39	0.42	0.36	0.37	0.40	0.41	0.37	0.42
MgO	11.62	11.49	11.85	13.67	13.99	13.52	13.31	11.35	11.76	11.42	15.14	14.60	14.95	14.31	15.20	14.71	15.26
CaO	10.68	10.73	9.96	10.45	10.63	10.29	10.54	10.65	10.59	10.51	11.17	11.16	11.07	11.21	11.27	11.44	11.14
Na_2O	1.94	1.84	1.90	1.65	1.63	1.79	1.69	2.05	1.87	1.85	2.59	2.71	2.57	2.67	2.57	2.59	2.59
K_2O	0.49	0.52	0.49	0.30	0.27	0.29	0.27	0.51	0.45	0.50	0.62	0.58	0.65	0.61	0.59	0.64	0.63
TOTAL	97.33	96.85	97.48	97.10	97.29	97.01	97.49	97.76	97.20	96.63	97.44	97.57	98.02	97.48	98.10	98.08	98.28
Geothermometers (ºC)																	
Ridolfi et al. (2010)-Eqn.1	-	-	-	850.52	838.40	856.74	859.81	-	-	-	944.88	955.61	929.28	947.66	927.85	948.63	930.80
Ridolfi & Renzulli (2012)-Eqn.2	-	-	-	863.86	852.82	885.51	858.39	-	-	-	1010.85	1030.54	995.94	1023.95	995.61	1001.37	1005.41
Amph-only-Putirka (2016)-Eqn.5	858.95	-	-	829.48	820.41	834.49	829.91	-	-	-	947.96	968.90	941.24	970.02	940.98	954.45	941.90
Geobarometers (kbar)																	
Ridolfi et al. (2010)-Eqn.4	-	-	-	2.10	1.76	2.16	2.38	-	-	-	1.86	2.22	1.92	2.31	1.84	2.06	1.85
Ridolfi & Renzulli (2012)-Eqn.1d	-	-	-	-	-	0.08	-	-	-	-	4.66	5.46	4.60	5.31	4.27	4.30	4.76

Table 2a-Appendix (continuation)

Mineral	Pl	Pl	Pl	Pl	Pl	Pl	Pl	Pl	Pl	Pl	Pl	Pl	Pl	Pl	Pl	Pl	Pl	Pl
Sample	G2-63	G2-63	G2-63	G2-63	G2-63	G2-63	G2-63	G2-63	G2-63	G2-63	G2-63	G2-63	G2-63	G2-63	G2-63	G2-63	G2-63	G2-63
Profile	profile 1	profile 1	profile 1	profile 1	profile 1	profile 1	profile 1	profile 1	profile 1	profile 1	profile 1	profile 1	profile 1	profile 1	profile 1	profile 2	profile 2	profile 2
Texture	rim	center	center	center	center	center	center	center	center	center	center	center	rim	rim	rim	rim	Albitic ring	center
Analysis	26 / 1	27 / 1	28 / 1	29 / 1	30 / 1	31 / 1	32 / 1	33 / 1	34 / 1	35 / 1	36 / 1	37 / 1	38 / 1	39 / 1	42 / 1 (A)	43 / 1	44 / 1	45 / 1
SiO_2	57.03	58.41	58.12	58.33	57.85	56.12	56.70	58.06	58.42	56.04	56.32	57.80	58.20	57.33	60.33	57.10	66.57	58.65
TiO_2	0.00	0.01	0.00	0.00	0.02	0.03	0.02	0.01	0.00	0.00	0.01	0.00	0.01	0.00	0.01	0.01	0.00	0.01
Al_2O_3	26.44	25.89	26.11	26.07	26.27	27.25	26.66	25.70	26.02	27.47	26.94	26.34	25.63	26.78	25.08	26.66	21.22	25.91
Cr_2O_3	0.00	0.00	0.01	0.00	0.01	0.00	0.00	0.04	0.01	0.00	0.02	0.01	0.00	0.00	0.00	0.00	0.02	0.01
NiO	0.00	0.00	0.02	0.01	0.00	0.00	0.00	0.04	0.06	0.02	0.03	0.00	0.00	0.02	0.03	0.00	0.02	0.00
FeOt	0.23	0.10	0.14	0.18	0.16	0.15	0.16	0.11	0.11	0.10	0.11	0.10	0.14	0.17	0.08	0.13	0.03	0.11
MnO	0.01	0.00	0.00	0.01	0.03	0.02	0.02	0.02	0.00	0.01	0.00	0.00	0.00	0.00	0.01	0.02	0.00	0.00
MgO	0.00	0.02	0.02	0.01	0.00	0.00	0.01	0.00	0.00	0.01	0.01	0.01	0.01	0.01	0.01	0.02	0.01	0.00
CaO	9.08	8.08	8.17	8.21	8.40	9.63	9.35	8.23	8.18	10.05	9.60	8.43	8.06	8.98	6.73	8.94	0.86	8.03
Na_2O	6.73	7.12	7.12	7.13	6.98	6.33	6.47	7.16	7.14	6.21	6.45	6.95	6.94	6.75	8.37	6.79	11.77	7.19
K_2O	0.18	0.25	0.24	0.27	0.24	0.18	0.21	0.24	0.25	0.18	0.19	0.25	0.25	0.20	0.22	0.23	0.01	0.28
TOTAL	99.71	99.88	99.94	100.22	99.98	99.69	99.60	99.62	100.20	100.09	99.67	99.88	99.25	100.25	100.86	99.89	100.52	100.19
xAN	0.42	0.38	0.38	0.38	0.39	0.45	0.43	0.38	0.38	0.46	0.44	0.39	0.38	0.41	0.30	0.41	0.38	0.37

Table 2b- Appendix

Mineral	Pl	Pl	Pl	Pl	Pl	Pl	Pl	Pl	Pl	Pl	Pl	Pl	Pl	Pl	Pl	Pl	Pl	Pl
Sample	G2-63	G2-63	G2-63	G2-63	G2-63	G2-63	G2-63	G2-63	G2-63	G2-63	G2-63	G2-63	G2-63	G2-63	G2-63	G2-63	G2-63	G3-157
Profile	profile 2	profile 2	profile 2	profile 2	profile 2	profile 3	profile 3	profile 3	profile 3	profile 3	profile 3	profile 3	profile 3	profile 3	profile 3	profile 3	profile 3	profile 1
Texture	center	center	center	center	rim	rim	Albitic ring	center	center	Albitic ring	center	center	center	center	center	center	center	rim
Analysis	46 / 1	47 / 1	48 / 1	49 / 1 (B)	50 / 1 (A)	51 / 1	52 / 1	53 / 1	54 / 1	55 / 1	56 / 1	57 / 1	58 / 1	59 / 1	60 / 1	61 / 1	62 / 1 (B)	13 / 1 (A)
SiO_2	57.93	58.76	58.12	58.09	57.36	57.52	67.96	57.41	56.64	66.62	58.17	58.03	58.64	57.72	58.44	53.93	57.07	60.46
TiO_2	0.02	0.02	0.04	0.02	0.01	0.00	0.01	0.00	0.00	0.00	0.01	0.01	0.01	0.01	0.00	0.01	0.01	0.05
Al_2O_3	26.30	25.45	25.88	25.74	26.68	26.36	20.58	26.16	26.74	20.66	26.04	25.91	26.24	26.91	26.18	29.00	26.81	24.10
Cr_2O_3	0.00	0.01	0.00	0.02	0.00	0.03	0.03	0.00	0.00	0.01	0.00	0.03	0.00	0.00	0.00	0.00	0.01	0.00
NiO	0.00	0.00	0.00	0.04	0.00	0.00	0.01	0.00	0.04	0.02	0.02	0.03	0.02	0.00	0.00	0.04	0.02	0.00
FeO_t	0.14	0.13	0.12	0.10	0.18	0.19	0.08	0.12	0.16	0.00	0.23	0.17	0.15	0.16	0.15	0.13	0.16	0.58
MnO	0.00	0.02	0.03	0.00	0.00	0.00	0.00	0.00	0.00	0.00	0.00	0.04	0.00	0.00	0.03	0.03	0.02	0.00
MgO	0.01	0.01	0.01	0.00	0.01	0.01	0.01	0.01	0.01	0.00	0.01	0.00	0.04	0.01	0.00	0.00	0.02	0.03
CaO	8.63	7.90	8.09	8.16	8.89	8.78	0.65	8.44	9.10	0.38	8.25	8.32	8.34	8.85	8.24	11.70	9.08	6.34
Na_2O	6.88	7.23	7.13	7.01	6.70	6.83	11.31	6.97	6.50	12.02	7.17	6.97	7.07	6.78	7.08	5.15	6.74	7.93
K_2O	0.23	0.25	0.23	0.23	0.20	0.22	0.05	0.23	0.20	0.03	0.24	0.26	0.23	0.23	0.23	0.14	0.18	0.67
TOTAL	100.14	99.79	99.65	99.41	100.04	99.94	100.69	99.35	99.40	99.74	100.14	99.78	100.73	100.67	100.35	100.11	100.13	100.17
xAN	0.40	0.37	0.38	0.38	0.41	0.41	0.308	0.39	0.43	0.17	0.38	0.39	0.38	0.41	0.38	0.55	0.42	0.29

Table 2b- Appendix (continuation)

Mineral	Pl	Pl	Pl	Pl	Pl	Pl	Pl	Pl	Pl	Pl	Pl	Pl	Pl	Pl	Pl	Pl	Pl	Pl
Sample	G3-157	G3-157	G3-157	G3-157	G3-157	G3-157	G3-157	G3-157	G3-157	G3-157	G3-157	G3-157	G3-157	G3-157	G3-157	G3-157	G3-157	G3-157
Profile	profile 1	profile 1	profile 1	profile 1	profile 2	profile 2	profile 2	profile 2	profile 2	profile 2	profile 3	profile 3	profile 3	profile 3	profile 3	profile 4	profile 4	profile 4
Texture	center	center	center	rim	rim	center	center	center	center	rim	rim	center	center	center	center	rim	center	center
Analysis	14 / 1	15 / 1	16 / 1	17 / 1 (B)	18 / 1 (A)	19 / 1	20 / 1	21 / 1	22 / 1	23 / 1 (B)	24 / 1 (A)	25 / 1	26 / 1	27 / 1	28 / 1 (B)	43 / 1 (A)	44 / 1	45 / 1
SiO_2	53.90	57.92	58.44	58.87	56.48	56.43	56.60	57.40	56.27	56.23	56.07	55.90	56.41	57.02	56.57	57.64	58.89	56.15
TiO_2	0.05	0.04	0.03	0.06	0.05	0.04	0.00	0.04	0.06	0.05	0.03	0.03	0.03	0.05	0.03	0.03	0.03	0.02
Al_2O_3	28.83	25.89	25.68	25.40	27.08	26.88	26.58	26.49	27.00	27.12	27.39	27.25	27.01	26.63	27.05	25.93	25.33	26.07
Cr_2O_3	0.00	0.00	0.00	0.00	0.02	0.00	0.01	0.02	0.00	0.00	0.01	0.03	0.02	0.00	0.00	0.00	0.00	0.01
NiO	0.00	0.00	0.00	0.00	0.00	0.00	0.00	0.00	0.00	0.00	0.02	0.01	0.01	0.02	0.07	0.00	0.00	0.00
FeO_t	0.47	0.52	0.45	0.48	0.50	0.47	0.49	0.49	0.49	0.47	0.45	0.53	0.51	0.53	0.45	0.41	0.47	0.47
MnO	0.00	0.00	0.04	0.00	0.03	0.04	0.01	0.00	0.00	0.06	0.03	0.04	0.04	0.02	0.00	0.00	0.00	0.05
MgO	0.03	0.04	0.03	0.04	0.05	0.05	0.05	0.05	0.06	0.04	0.05	0.05	0.05	0.05	0.04	0.04	0.03	0.03
CaO	11.60	8.30	8.06	7.69	9.66	9.57	9.31	8.96	9.68	9.65	9.83	9.84	9.56	9.05	9.44	8.28	7.60	8.83
Na_2O	5.10	6.82	7.15	7.33	6.22	6.19	6.46	6.63	6.24	6.14	6.05	6.06	6.25	6.51	6.31	6.91	7.33	6.21
K_2O	0.24	0.47	0.41	0.51	0.30	0.33	0.35	0.33	0.32	0.33	0.28	0.30	0.32	0.35	0.31	0.30	0.49	0.37
TOTAL	100.22	99.99	100.28	100.38	100.39	100.00	99.87	100.41	100.13	100.10	100.20	100.03	100.20	100.24	100.26	99.54	100.17	98.21
xAN	0.54	0.39	0.37	0.35	0.45	0.45	0.43	0.41	0.45	0.45	0.46	0.46	0.45	0.42	0.44	0.39	0.35	0.43

Table 2b- Appendix (continuation)

Mineral	**Pl**	**Pl**	**Pl**	**Pl**	**Pl**	**Pl**	**Pl**	**Pl**	**Pl**	**Pl**	**Pl**	**Pl**	**Pl**	**Pl**	**Pl**	**Pl**	**Pl**	**Pl**	**Pl**
Sample	**G3-157**	**G3-157**	**G3-157**	**G3-157**	**G3-157**	**G3-157**	**G3-157**	**G3-157**	**G3-157**	**G3-157**	**G3-157**	**G3-157**	**G3-157**	**G3-157**	**G3-157**	**G3-157**	**G3-157**	**G3-157**	**G3-157**
Profile	**profile 4**	**profile 4**	**profile 4**	**profile 4**	**profile 4**	**profile 4**	**profile 4**	**profile 4**	**profile 4**	**profile 4**	**profile 5**	**profile 5**	**profile 5**	**profile 5**	**profile 5**	**profile 5**	**profile 5**	**profile 5**	**profile 5**
Texture	**center**	**center**	**center**	**center**	**center**	**center**	**center**	**center**	**center**	**rim**	**rim**	**center**	**center**	**center**	**center**	**center**	**center**	**center**	**center**
Analysis	**46 / 1**	**47 / 1**	**48 / 1**	**49 / 1**	**50 / 1**	**51 / 1**	**52 / 1**	**53 / 1**	**54 / 1**	**55 / 1 (B)**	**62 / 1 P1**	**63 / 1**	**64 / 1**	**65 / 1**	**66 / 1**	**67 / 1**	**68 / 1**	**69 / 1**	**70 / 1 P9**
SiO_2	58.59	56.06	53.61	56.05	57.11	55.31	58.01	57.65	56.78	56.55	56.35	57.56	56.59	56.14	55.92	55.71	57.55	55.74	58.28
TiO_2	0.03	0.06	0.06	0.03	0.03	0.07	0.04	0.02	0.06	0.05	0.04	0.04	0.02	0.06	0.05	0.03	0.05	0.02	0.01
Al_2O_3	25.77	27.42	28.55	27.51	26.73	27.60	26.03	26.05	26.74	27.02	26.93	26.01	26.62	27.11	27.40	27.27	26.22	27.41	25.86
Cr_2O_3	0.00	0.01	0.01	0.05	0.00	0.02	0.00	0.01	0.02	0.01	0.01	0.00	0.00	0.05	0.00	0.00	0.01	0.00	0.01
NiO	0.01	0.04	0.02	0.00	0.02	0.00	0.00	0.00	0.00	0.01	0.06	0.01	0.03	0.00	0.00	0.00	0.06	0.04	0.02
FeO_t	0.36	0.43	0.65	0.46	0.32	0.46	0.50	0.52	0.46	0.49	0.51	0.49	0.48	0.49	0.48	0.51	0.50	0.45	0.34
MnO	0.03	0.00	0.04	0.01	0.02	0.00	0.03	0.04	0.01	0.00	0.00	0.01	0.01	0.00	0.03	0.00	0.03	0.00	0.00
MgO	0.03	0.04	0.03	0.04	0.02	0.04	0.04	0.05	0.04	0.05	0.03	0.05	0.04	0.04	0.05	0.05	0.04	0.05	0.03
CaO	7.81	9.75	11.68	9.84	9.05	10.30	8.38	8.53	9.43	9.54	9.56	8.72	9.49	9.73	10.00	10.01	8.68	10.15	8.27
Na_2O	7.29	6.06	5.05	6.12	6.49	5.94	6.88	6.74	6.33	6.28	6.22	6.64	6.25	6.16	5.90	5.89	6.57	5.82	7.00
K_2O	0.35	0.31	0.18	0.30	0.18	0.28	0.40	0.40	0.33	0.30	0.34	0.41	0.37	0.34	0.28	0.34	0.41	0.30	0.39
TOTAL	100.28	100.17	99.88	100.40	99.98	100.03	100.32	100.00	100.20	100.30	100.06	99.95	99.89	100.12	100.11	99.82	100.12	99.97	100.22
xAN	0.36	0.46	0.55	0.46	0.43	0.48	0.39	0.40	0.44	0.44	0.45	0.41	0.44	0.45	0.47	0.47	0.41	0.48	0.38

Table 2b-Appendix (continuation)

Mineral	**Cpx**	**Cpx**	**Cpx**	**Cpx**	**Cpx**	**Cpx**	**Cpx**	**Cpx**	**Cpx**	**Cpx**	**Cpx**
Sample	**G3-157**	**G3-157**	**G3-157**	**G3-157**	**G3-157**	**G3-157**	**G3-157**	**G3-157**	**G3-157**	**G3-157**	**G3-157**
Profile	**profile 1**	**profile 1**	**profile 1**	**profile 1**	**profile 1**	**profile 1**	**profile 1**	**profile 2**	**profile 2**	**profile 2**	**profile 2**
Texture	**rim**	**center**	**center**	**center**	**center**	**center**	**rim**	**rim**	**center**	**center**	**center**
Analysis	**3 / 1**	**4 / 1**	**5 / 1**	**6 / 1**	**7 / 1**	**8 / 1**	**9 / 1**	**33 / 1**	**34 / 1**	**35 / 1**	**36 / 1**
SiO_2	52.53	52.90	52.55	52.36	52.38	52.33	52.65	51.27	51.64	51.54	50.95
TiO_2	0.45	0.41	0.47	0.51	0.49	0.52	0.48	0.81	0.75	0.79	0.82
Al_2O_3	1.01	1.07	1.23	1.39	1.37	1.56	1.63	2.66	2.27	2.48	2.82
Cr_2O_3	0.02	0.01	0.03	0.00	0.00	0.00	0.00	0.00	0.00	0.02	0.01
NiO	0.05	0.07	0.00	0.00	0.01	0.00	0.02	0.07	0.02	0.01	0.04
FeO_t	8.94	8.82	8.59	8.58	8.32	8.16	8.10	8.24	8.28	8.19	8.05
MnO	0.82	0.74	0.62	0.62	0.56	0.51	0.57	0.26	0.40	0.28	0.29
MgO	15.36	15.63	15.37	15.46	15.47	15.46	15.39	15.70	15.79	15.70	15.45
CaO	20.52	20.90	20.99	20.82	21.32	21.37	21.72	21.03	20.85	20.96	21.19
Na_2O	0.51	0.48	0.46	0.42	0.40	0.42	0.37	0.35	0.34	0.39	0.39
K_2O	0.00	0.00	0.01	0.00	0.01	0.02	0.00	0.00	0.00	0.00	0.00
TOTAL	100.21	101.02	100.32	100.16	100.34	100.36	100.94	100.38	100.35	100.35	100.01
Temperature-dependent geobarometer in Cpx given by equation 32a of Putirka (2008) using temperature of Putirka (2016)-Eqn.5 (kbar)	-	-	-	-	-	-	-	2.01	1.30	2.26	2.51

Table 2c-Appendix

Mineral	**Cpx**	**Cpx**	**Cpx**	**Cpx**	**Cpx**	**Cpx**	**Cpx**	**Cpx**	**Cpx**	**Cpx**	**Cpx**
Sample	**G3-157**	**G3-157**	**G3-157**	**G3-157**	**G3-157**	**G3-157**	**G3-157**	**G3-157**	**G3-157**	**G3-157**	**G3-157**
Profile	**profile 2**	**profile 2**	**profile 2**	**profile 2**	**profile 2**	**profile 3**	**profile 3**	**profile 3**	**profile 3**	**profile 3**	**profile 3**
Texture	**center**	**center**	**center**	**rim**	**rim**	**rim**	**center**	**center**	**center**	**center**	**rim**
Analysis	**37 / 1**	**38 / 1**	**39 / 1**	**40 / 1**	**41 / 1**	**56 / 1**	**57 / 1**	**58 / 1**	**59 / 1**	**60 / 1**	**61 / 1**
SiO_2	50.87	51.25	51.17	50.73	50.79	53.23	51.11	51.01	50.56	50.72	51.28
TiO_2	1.02	0.80	0.86	0.89	0.82	0.30	0.76	0.76	0.87	0.82	0.71
Al_2O_3	3.02	2.36	2.70	2.79	2.78	1.39	2.98	3.01	3.07	3.01	2.27
Cr_2O_3	0.01	0.00	0.01	0.02	0.02	0.04	0.00	0.00	0.00	0.00	0.01
NiO	0.00	0.00	0.00	0.02	0.00	0.02	0.00	0.01	0.00	0.00	0.00
FeO_t	8.28	8.06	8.35	8.15	8.18	9.17	7.98	8.11	8.05	8.03	7.91
MnO	0.30	0.30	0.34	0.31	0.21	0.54	0.20	0.23	0.25	0.19	0.30
MgO	15.35	15.80	15.67	15.21	15.33	14.96	15.16	15.35	15.11	15.17	15.47
CaO	20.98	20.53	20.76	21.36	20.94	20.25	21.56	21.47	21.46	21.50	21.12
Na_2O	0.38	0.36	0.36	0.39	0.40	0.24	0.31	0.31	0.36	0.34	0.36
K_2O	0.00	0.00	0.00	0.00	0.00	0.01	0.00	0.00	0.00	0.01	0.00
TOTAL	100.21	99.45	100.20	99.87	99.47	100.16	100.07	100.26	99.72	99.80	99.44
Temperature-dependent geobarometer in Cpx given by equation 32a of Putirka (2008) using temperature of Putirka (2016)-Eqn.5 (kbar)	2.90	2.17	2.39	1.86	2.96	3.38	2.82	2.53	2.54	2.47	1.59

Table 2c-Appendix (continuation)

Mineral	**Mag**	**Mag**	**Usp**	**Mag**	**Usp**	**Mag**	**Mag**	**Usp**	**Mag**	**Mag**	**Mag**
Sample	**G2-63**	**G2-63**	**G2-63**	**G2-63**	**G2-63**	**G3-157**	**G3-157**	**G3-157**	**G3-157**	**G3-157**	**G3-157**
Analysis	**14 / 1**	**15 / 1**	**22 / 1**	**40 / 1**	**68 / 1**	**69 / 1**	**1 / 1**	**2 / 1**	**10 / 1**	**30 / 1**	**31 / 1**
SiO_2	0.05	0.65	0.00	1.49	0.01	0.06	0.09	0.02	0.07	0.08	0.07
TiO_2	4.01	1.20	30.46	14.12	30.03	2.43	2.48	30.51	4.44	2.99	3.35
Al_2O_3	2.12	1.13	0.35	1.02	0.29	1.70	2.65	0.01	3.08	3.82	3.82
Cr_2O_3	0.33	0.23	0.06	0.35	0.09	0.32	0.02	0.01	0.00	0.22	0.03
NiO	0.02	0.01	0.00	0.06	0.03	0.00	0.03	0.04	0.03	0.04	0.01
FeO_t	86.28	91.49	65.32	72.29	64.56	89.89	89.58	61.77	84.63	86.54	90.28
MnO	0.49	0.39	0.35	3.42	0.79	0.82	0.28	0.44	0.03	0.06	0.16
MgO	1.33	0.07	1.24	1.03	1.23	0.41	0.03	0.03	0.00	0.01	0.04
CaO	0.03	0.51	0.03	1.43	0.04	0.02	0.01	0.39	0.02	0.00	0.02
Na_2O	0.00	0.00	0.00	0.00	0.00	0.00	0.02	0.00	0.00	0.02	0.00
K_2O	0.00	0.00	0.00	0.00	0.00	0.00	0.00	0.00	0.00	0.00	0.00
TOTAL	94.67	95.67	97.81	95.21	97.08	95.66	95.21	93.22	92.31	93.80	97.78

Table 2d-Appendix

Mineral	Amp	Amp	Amp	Amp	Amp	Amp
Sample	**T1-1**	**T1-2**	**T0**	**G2-63-1**	**G2-63-2**	**G3-134**
Major oxides in wt%						
SiO_2	46.40	45.72	47.60	46.78	46.89	42.95
TiO_2	1.73	1.12	1.95	0.92	1.14	2.39
Al_2O_3	15.53	14.89	13.64	13.09	12.98	14.23
FeO_t	10.07	14.15	12.21	14.35	14.13	10.49
MnO	0.14	0.33	0.17	0.36	0.33	0.11
MgO	10.75	8.91	8.85	9.89	10.17	12.48
CaO	11.34	10.93	11.04	10.89	10.49	11.93
Na_2O	2.48	1.98	2.75	1.69	1.84	2.23
K_2O	0.19	0.22	0.13	0.19	0.24	0.41
P_2O_5	0.02	0.02	0.01	0.07	0.02	0.03
LOI	0.05	0.05	0.05	0.05	0.11	1.15
Total	99.80	99.82	99.78	99.85	99.82	99.63
Trace elements in ppm						
U	0.01	0.04	0.29	0.02	0.03	0.03
Th	0.06	0.10	0.52	0.08	0.12	0.13
Zr	39.00	41.12	76.60	40.50	54.20	77.50
Hf	1.77	2.15	3.14	2.24	2.72	3.53
Ta	0.09	0.10	0.31	0.11	0.14	0.20
Nb	2.20	4.00	6.10	4.38	5.37	4.09
Y	26.25	56.50	35.23	56.60	41.90	24.85
Ba	114.50	85.20	161.80	44.60	77.80	207.80
Sr	247.70	101.20	277.90	61.40	80.20	519.00
Cs	0.02	0.03	0.06		0.01	0.09
Rb	2.37	1.40	1.26	0.71	1.54	3.76
Sb	0.24	0.13	0.18	0.09	0.08	0.07
Cr	249.50	38.00	423.30	59.60	301.10	612.00
Co	62.60	52.30	47.20	54.40	57.20	75.50
Ni	149.70	52.60	137.60	50.70	103.60	584.00
Sc	76.91	58.80	84.20	57.80	56.70	81.90
La	3.31	8.76	8.68	10.91	13.47	6.64
Ce	12.54	41.30	26.48	49.30	44.00	21.72
Pr	2.75	9.57	4.62	10.75	8.24	4.49
Nd	15.54	58.20	23.33	58.90	42.00	27.90
Sm	5.11	18.33	7.20	15.55	10.35	8.10
Eu	1.43	3.93	1.98	3.51	2.60	2.33
Gd	5.75	16.08	7.74	14.37	9.60	7.82
Tb	0.90	2.14	1.12	1.90	1.38	1.05
Dy	5.16	11.64	7.03	11.42	7.98	5.60
Ho	1.03	2.25	1.39	2.15	1.59	1.02
Er	2.77	5.90	4.04	6.03	4.66	2.55
Tm	0.38	0.78	0.68	0.80	0.65	0.29
Yb	2.19	4.56	6.11	5.10	4.00	1.67
Lu	0.33	0.69	1.27	0.72	0.60	0.25
Pb	1.02	1.49	3.79	1.12	1.31	3.17
Ga	16.20	26.74	16.40	25.41	24.54	15.70
Eu/Eu*	0.80	0.70	0.81	0.72	0.80	0.89
Nb/Ta	23.91	38.46	19.93	39.11	38.91	20.35
Geothermometers (°C)						
Ridolfi et al. (2010)-Eqn.1	950	902	904	861	858	981
Ridolfi & Renzulli (2012)-Eqn.2	859	812	805	785	809	893
Amph-only-Putirka (2016)-Eqn.5	915	853	876	819	828	953
Geobarometers (kbar)						
Ridolfi et al. (2010)-Eqn.4	8.40	7.50	5.69	4.74	4.56	6.51
Ridolfi & Renzulli (2012)-Eqn.1d	10.46	6.25	10.33	2.20	3.68	6.09

Mineral	Amp	Amp	Amp	Amp	Amp	Amp	Amp	Amp	Amp	Amp	Amp	Amp	Amp	Amp	Amp
Sample	JZ6-4	JZ6-4	JZ6-4	JZ6-4	JZ6-4	JZ6-4	JZ6-4	JZ6-4	JZ6-4	JZ6-4	JZ6-4	JZ6-4	JZ6-4	JZ6-4	JZ6-4
Profile	profile 1	profile 1	profile 1	profile 2	profile 2	profile 2	profile 2	profile 2	profile 2	profile 2	profile 3	profile 3	profile 3	profile 3	profile 3
Analysis	1-3	1-4	1-5	2-1	2-2	2-3	2-4	2-6	2-7	2-8	3-1	3-2	3-3	3-4	3-5	3-6
Texture	center	center	center	rim	center	center	center	center	center	rim	rim	center	center	center	center	center
SiO_2	47.68	47.74	43.20	48.91	47.67	47.35	47.98	47.48	48.59	49.55	47.37	49.30	47.33	46.97	46.89	47.34
TiO_2	2.97	2.40	3.37	2.22	2.27	2.58	2.59	3.25	2.10	5.76	1.32	1.36	1.83	2.27	2.48	2.53
Al_2O_3	11.29	12.07	22.24	12.61	11.55	11.59	11.74	11.43	11.76	13.73	13.32	10.59	11.61	11.94	12.45	11.56
FeO_t	11.94	12.09	11.22	13.54	14.15	13.55	12.75	13.38	14.98	15.41	13.66	12.65	13.96	14.33	13.52	13.94
MgO	12.71	11.84	9.23	10.23	11.26	11.42	12.08	11.85	10.51	10.66	11.11	12.59	11.54	11.41	11.31	11.66
CaO	10.51	11.58	10.35	10.30	10.35	11.39	10.37	10.33	9.58	4.83	10.90	11.22	11.02	10.75	11.12	10.81
Na_2O	2.22	1.69	0.00	1.66	2.41	1.63	1.97	1.64	2.00	0.00	1.83	1.83	2.06	1.97	1.83	1.73
K_2O	0.68	0.59	0.39	0.54	0.34	0.49	0.53	0.64	0.47	0.06	0.49	0.46	0.65	0.36	0.41	0.43
TOTAL	100.00	100.00	100.00	100.00	100.00	100.00	100.00	100.00	100.00	100.00	100.00	100.00	100.00	100.00	100.00	100.00

Mineral	Amp	Amp	Amp	Amp	Amp	Amp	Amp	Amp	Amp	Amp	Amp	Amp
Sample	JZ6-4	JZ6-4	G2-63	G2-63	G2-63	G2-63	G2-63	G2-63	G2-63	G2-63	G2-63	G2-63
Profile	profile 3	profile 3	profile 1	profile 1	profile 1	profile 1	profile 2	profile 2	profile 2	profile 2	profile 2	profile 2
Analysis	3-7	3-8	1-1	1-4	1-6	1-7	2-1	2-2	2-3	2-4	2-5	2-7
Texture	center	rim	rim	center	center	rim	rim	center	center	center	center	rim
SiO_2	47.09	46.72	47.02	46.91	48.25	47.38	48.41	46.36	46.25	48.42	46.32	47.41
TiO_2	2.23	2.21	1.37		1.17	1.46						
Al_2O_3	11.48	12.07	10.51	10.65	9.60	9.99	9.45	11.43	12.11	9.95	11.51	10.50
FeO_t	13.95	14.57	14.09	14.00	12.81	13.03	13.01	14.43	14.16	14.00	14.38	13.62
MgO	11.63	10.90	14.18	14.16	14.98	14.26	14.98	13.42	12.76	14.16	13.00	14.72
CaO	10.95	11.22	10.85	10.81	10.81	11.36	10.98	11.12	10.94	10.77	11.22	10.81
Na_2O	1.95	1.98	1.60	1.85	1.59	1.66	1.62	1.63	1.73	1.50	1.67	1.69
K_2O	0.72	0.31	0.39	0.50	0.37	0.35	0.00	0.00	0.50	0.00	0.37	0.37
TOTAL	100.00	100.00	100.00	100.00	100.00	100.00	100.00	100.00	100.00	100.00	100.00	100.00

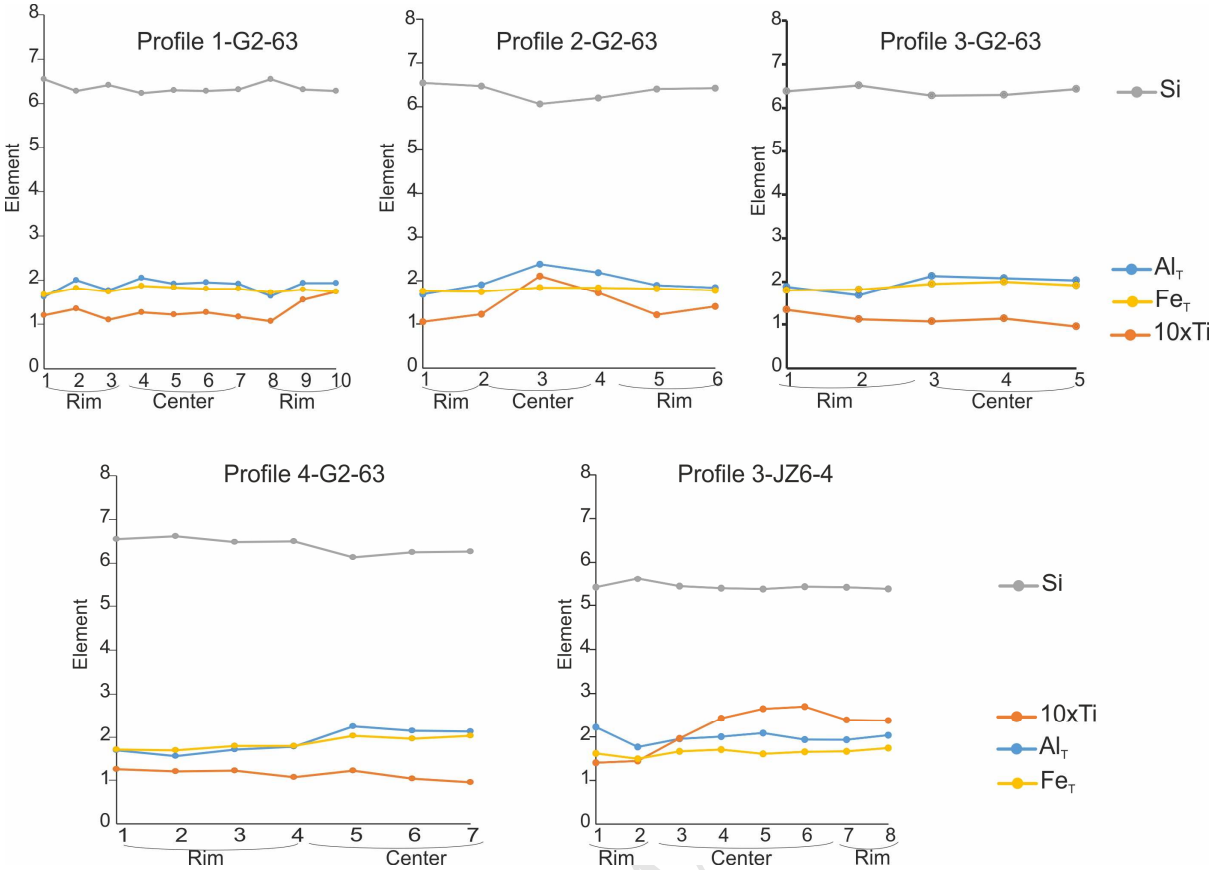

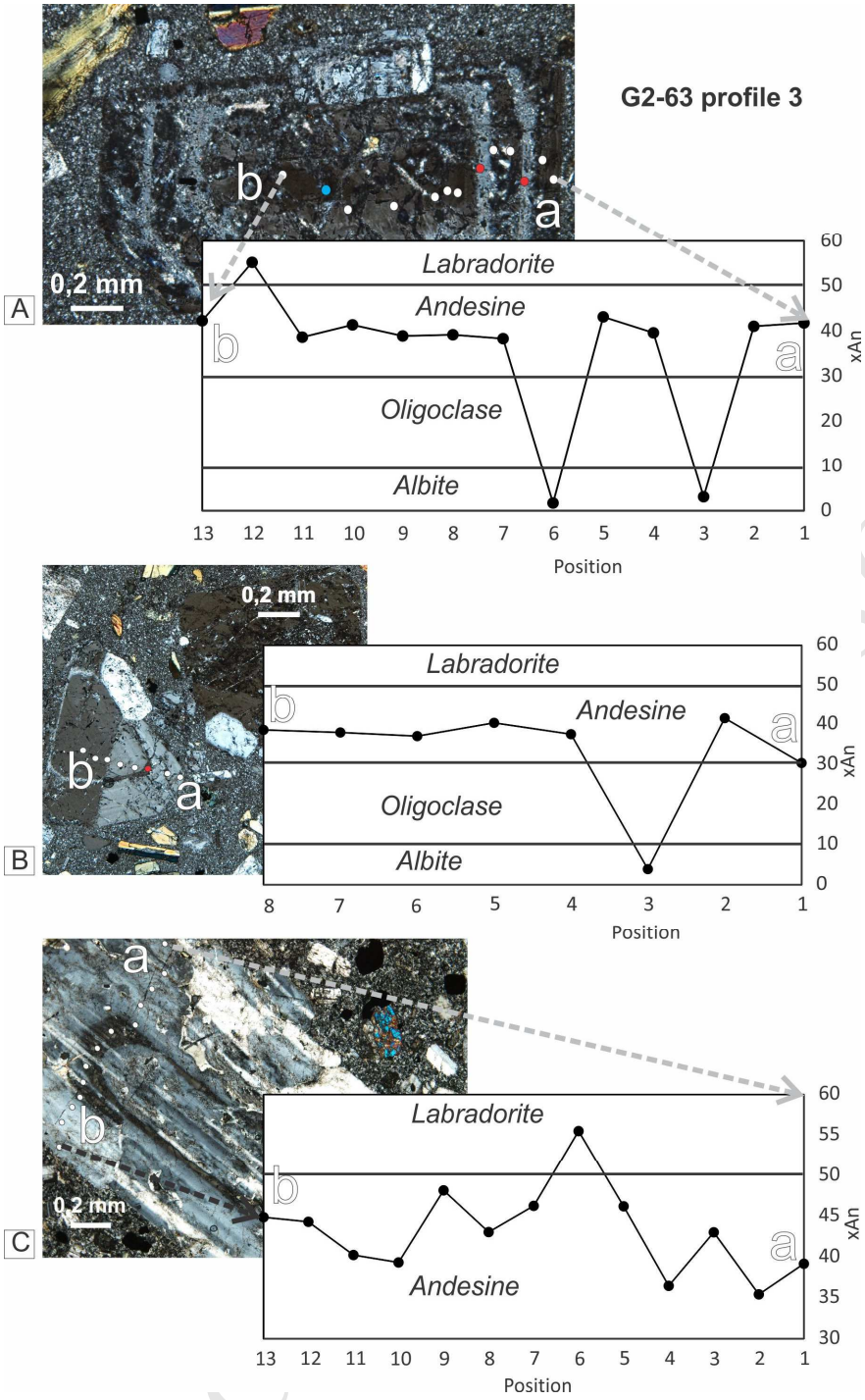

Analysis type		T1	T0	G2-63	G3-134	JZ6-4	G3-157
Lithology		**Amp-bearing trachydacite**	**Amp-bearing dacite**	**Amp-bearing dacite**	**Amp-bearing andesite**	**Amp-bearing andesite**	**Cpx-bearing trachydacite**
Outcrop		**Lava flow**	**Lava flow**	**Porphyry**	**Dike**	**Lava flow**	**Lava flow**
Latitude (degrees, South)		42.1307	41.8500	42.1244	42.2769	41.8800	42.1318
Longitude (degrees, West)		69.0719	69.3000	69.0335	69.3334	69.3660	69.3705
Whole-rock major analysis		Actlabs	Actlabs	SGS Peru	SGS Peru	-	SGS Peru
Age constraints		^{40}Ar-^{39}Ar Amp and paleomagnetic data in Zaffarana & Somoza (2012)		^{40}Ar-^{39}Ar Amp-SERNAGEOMIN	K-Ar whole rock-Actlabs	Form part of the paleomagnetic data defining an Early Jurassic paleopole (Zaffarana & Somoza, 2012)	-
		185 ± 1.6 / 184 ± 5	185.4 ± 2	178.9 ± 1.1	191.6 ± 5.2		
Mineral analysis	Electron microprobe	-	-	Pl, Amp, Mag, Usp	-	-	Pl, Cpx, Amp, Mag, Usp
	EDS data	-	-	Amp	-	Amp	-
	ICP-MS data	Amp	Amp	Amp	Amp	-	-

Element/ratio	La			Yb			$[La/Yb]_n$ melt			$[La/Yb]_n$	Sm		Eu			Gd		Eu/Eu* melt		Eu/Eu*
Melt/material	andesite	dacite	rhyolite	andesite	dacite	rhyolite	andesitic	dacitic	rhyolitic	whole rock	andesite	dacite	andesite	dacite	rhyolite	andesite	dacite	andesitic	dacitic	whole rock
Kd	0.48	0.26	1.92	2.73	1.31	5.5					3.85	2.38	1.9	5.9	3.2	1.72	2			
Reference	*1*			*1*							*1*		*2*	*3*	*2*	*4*	*3*			
T1-1	3.31	3.31	3.31	2.19	2.19	2.19					5.11	5.11	1.43	1.43	1.43	5.75	5.75			
T1-2	8.76	8.76	8.76	4.56	4.56	4.56					18.33	18.33	3.93	3.93	3.93	16.08	16.08			
T1-average	6.04	6.04	6.04	3.38	3.38	3.38					11.72	11.72	2.68	2.68	2.68	10.92	10.92			
Cmelt (T1)	12.57	23.21	3.14	1.24	2.58	0.61	6.91	6.12	3.48	11.20	3.04	4.92	1.41	0.45	0.84	6.35	5.46	0.98	0.27	0.91
T0	8.68	8.68	8.68	6.11	6.11	6.11					7.20	7.20	1.98	1.98	1.98	7.74	7.74			
Cmelt (T0)	18.08	33.38	4.52	2.24	4.66	1.11	5.49	4.86	2.76	12.80	1.87	3.03	1.04	0.34	0.62	4.50	3.87	1.10	0.30	0.96
G2-63-1	10.91	10.91	10.91	5.10	5.10	5.10					15.55	15.55	3.51	3.51	3.51	14.37	14.37			
G2-63-2	13.47	13.47	13.47	4.00	4.00	4.00					10.35	10.35	2.60	2.60	2.60	9.60	9.60			
G2-63-average	12.19	12.19	12.19	4.55	4.55	4.55					12.95	12.95	3.06	3.06	3.06	11.99	11.99			
Cmelt (G2-63)	25.40	46.88	6.35	1.67	3.47	0.83	10.35	9.17	5.21	12.10	3.36	5.44	1.61	0.52	0.95	6.97	5.99	1.01	0.28	1.08
G3-134-amp	6.64	6.64	6.64	1.67	1.67	1.67					8.10	8.10	2.33	2.33	2.33	7.82	7.82			
Cmelt (G3-134)	13.83	25.54	3.46	0.61	1.27	0.30	15.36	13.61	7.74	13.80	2.10	3.40	1.23	0.39	0.73	4.55	3.91	1.21	0.33	0.89

Sample name				G2-63			T0	T1	G3-134	G3-157	
Rock type (dominant mafic mineral)				**Amp-bearing volcanic rocks**						**Cpx-trachydacite** (Amp microphenocrysts)	
Analyzed material				**Cores**	**Rims**	**Single crystal**	**Single crystal**	**Single crystal**	**Single crystal**	**Cores**	**Rims**
Calibration			**Calibration uncertainty**								
Geothermometers (° C)	**Amp-Pl thermometer (Holland & Blundy 1994-expression B)**		±40°C	773-720	-	-	-	-	-	-	-
	Amphibole data (available in Tables 2 and 3 in the Appendix)	**Amp-only thermometer of Ridolfi et al. (2010)-Eqn.1**	±35°C	916	848	-	-	-	-	949	929
		Amp-only thermometer of Ridolfi & Renzulli (2012)-Eqn. 2	±32°C	901	867	-	-	-	-	1017	999
		Amp-only thermometer of Putirka (2016)-Eqn.5	±30°C	869	826	-	-	-	-	960	941
	Whole-rock data (available in Table 1-Appendix)	**Liquid-only-Molina et al. (2015)**	±35 to ±45°C	1032			992	1052	1041	991	
		Liquid-only-Putirka (2016)-Eqn.3	±33°C	991			960	1002	1008	1002	
		Zr-saturation T(°C)-Harrison&Watson (1983)	-	730			740	644	722	725	
		Zr-saturation T(°C)-Boehnke et al. (2013)	-	648			659	569	652	655	
		Ap-saturation T(°C)-Harrison&Watson (1984)	-	1026			910	877	851	847	
Geobarometers (kbar)	**Amphibole data (available in Tables 2 and 3 in the Appendix)**	**Hammarstrom & Zen (1986)**	±3 kbar	6.29-4.90	5.1	-	-	-	-	4.5	4
		Hollister et al. (1987)	±1 kbar	7.1	5.3	-	-	-	-	4.6	4.2
		Johnson & Rutherford (1989)	±0.5 kbar	7.6	4.1±0.69	-	-	-	-	3.6	3.2
		Schmidt (1992)	±0.6 kbar	5.8±0.75	5.7±0.64	-	-	-	-	4.9	4.5
		Ridolfi et al. (2010)-Eqn. 4	±0.39 kbar	7.4	2.2±0.40	-	-	-	-	2.1	1.9
		Ridolfi & Renzulli (2012)-Eqn.1d	±2.5 kbar	-	1.65	-	-	-	-	4.93	4.55
	Amp-Pl barometer (Molina et al., 2015) at T1*		±1.5 to ±2.3 kbar	7.6	3.5	-	-	-	-	-	-
	Amp-Pl barometer (Molina et al., 2015) at T2**			8.2	3.9	-	-	-	-	-	-
	Clinopyroxene data (available in Table 2-Appendix)	**Temperature-dependent geobarometer in Cpx given by equation 32a of Putirka (2008) using temperature of Putirka (2016)-Eqn.5**	±3.1 kbar	-	-	-	-	-	-	2	

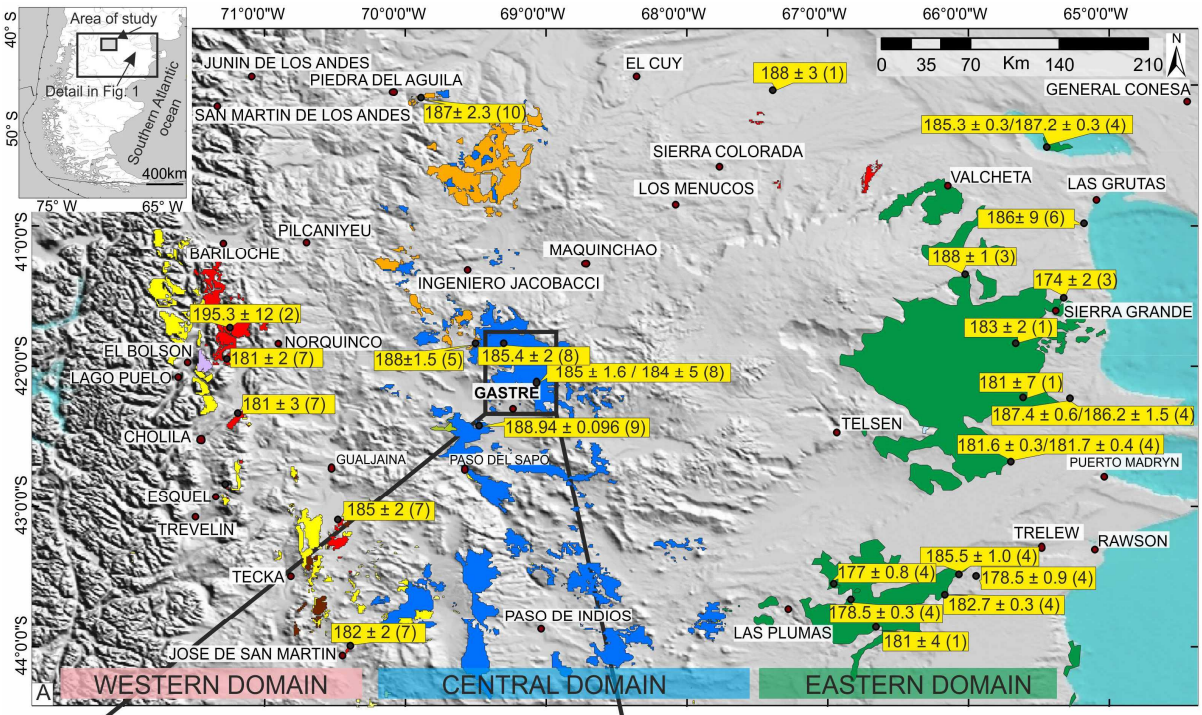

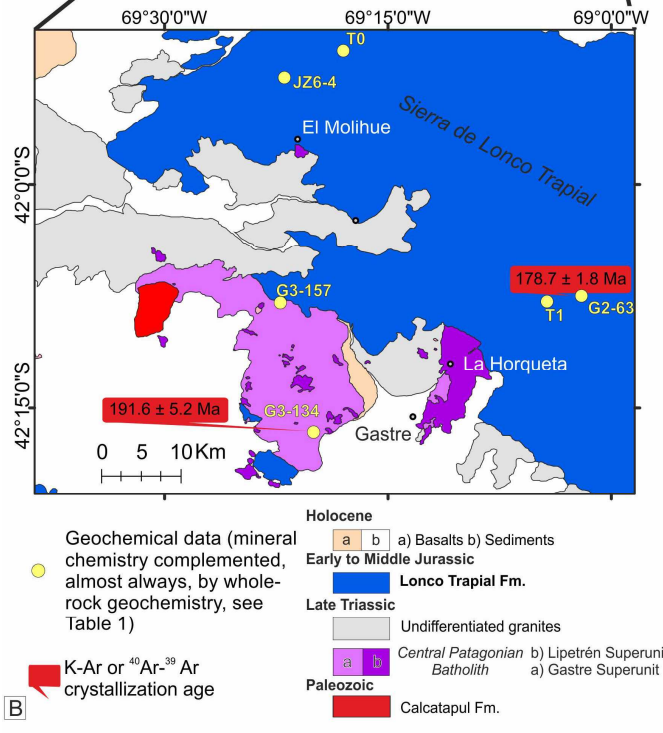

Geochemical data (mineral chemistry complemented, almost always, by whole-rock geochemistry, see Table 1)

K-Ar or ^{40}Ar-^{39} Ar crystallization age

Holocene

a) Basalts b) Sediments

Early to Middle Jurassic

Lonco Trapial Fm.

Late Triassic

Undifferentiated granites

Central Patagonian Batholith b) Lipetrén Superunit a) Gastre Superunit

Paleozoic

Calcatapul Fm.

GEOLOGICAL REFERENCES OF THE REGIONAL MAP OF EARLY JURASSIC UNITS OF THE NORTH PATAGONIAN MASSIF (Fig. 1A)

Eastern domain

Acidic and intermediate volcanites: Marifil Formation

Felsic intrusives: (El Sótano Granodiorite, Flores Granite)

Central domain

Andesitic volcanic dominated facies: Lonco Trapial, Taquetrén, Cerro Carnerero, Cañadón Puelman and Cajón de Ginebra formations

Dacites and rhyolites: Garamilla Formation

Sedimentary rocks: Las Leoneras, Los Tobianos, Puesto Lizarralde formations

Western domain

Felsic intrusives: Subcordilleran Plutonic Belt (Leleque Fm., Aleusco Granite)

Mafic and ultramafic intrusives: Tecka and Cresta de los Bosques formations

Sedimentary rocks: Piltriquitrón, Lepá, Osta Arena formations

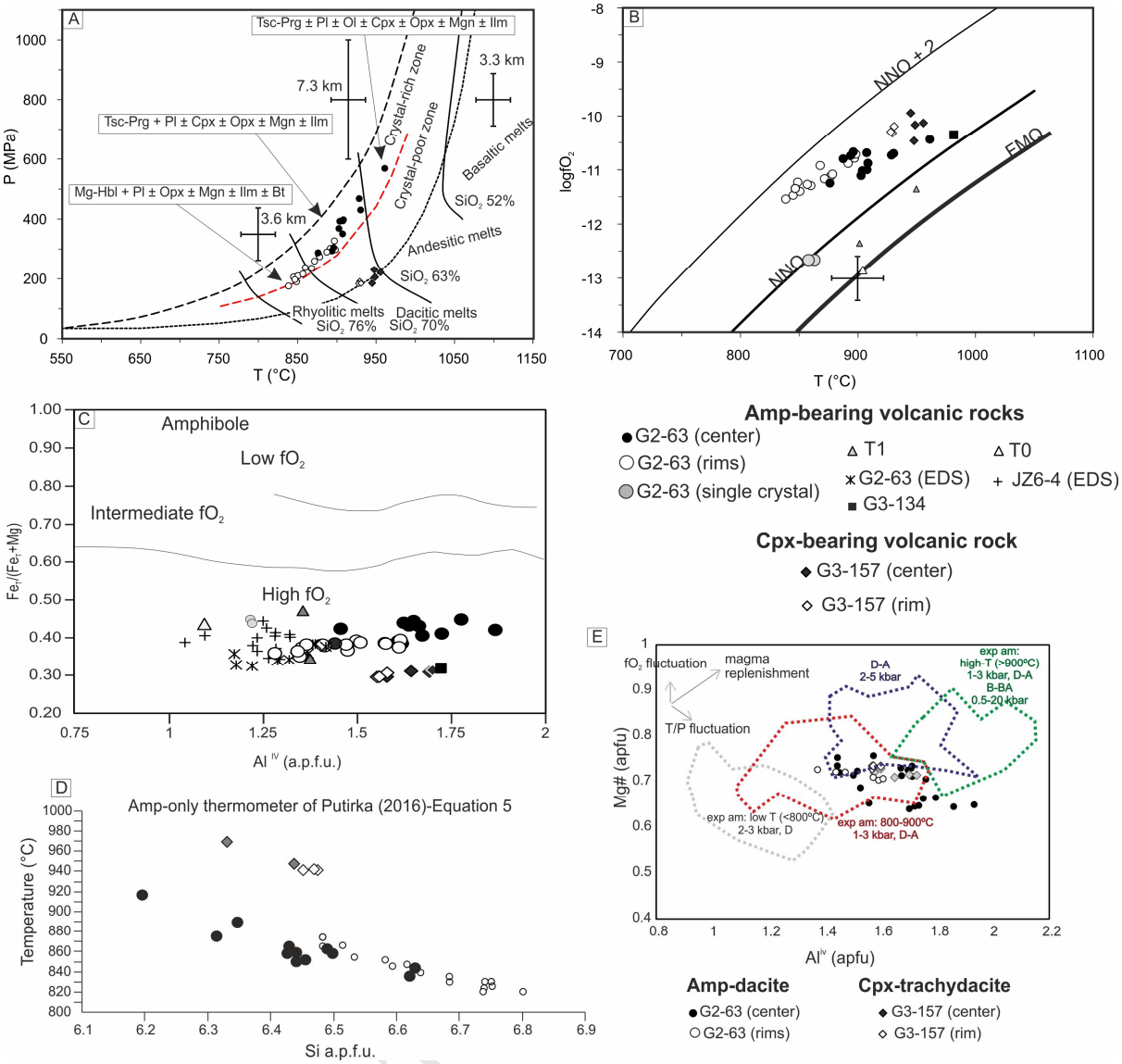
A
Tsc-Prg ± Pl ± Ol ± Cpx ± Opx ± Mgn ± Ilm
Tsc-Prg + Pl ± Cpx ± Opx ± Mgn ± Ilm
Mg-Hbl + Pl ± Opx ± Mgn ± Ilm ± Bt
7.3 km
3.3 km
3.6 km
Crystal-rich zone
Crystal-poor zone
Basaltic melts
Andesitic melts
SiO2 52%
SiO2 63%
Rhyolitic melts SiO2 76%
Dacitic melts SiO2 70%
P (MPa)
T (°C)
B
NNO + 2
NNO
FMQ
logfO2
T (°C)
Amp-bearing volcanic rocks
G2-63 (center)
G2-63 (rims)
G2-63 (single crystal)
T1
T0
G2-63 (EDS)
JZ6-4 (EDS)
G3-134
Cpx-bearing volcanic rock
G3-157 (center)
G3-157 (rim)
C
Amphibole
Low fO2
Intermediate fO2
High fO2
Fe3/(Fe3+Mg)
Al IV (a.p.f.u.)
D
Amp-only thermometer of Putirka (2016)-Equation 5
Temperature (°C)
Si a.p.f.u.
E
fO2 fluctuation
magma replenishment
T/P fluctuation
D-A 2-5 kbar
exp am: high-T (>900ºC) 1-3 kbar, D-A B-BA 0.5-20 kbar
exp am: low T (<800ºC) 2-3 kbar, D
exp am: 800-900ºC 1-3 kbar, D-A
Mg# (apfu)
Alᴵᵛ (apfu)
Amp-dacite
G2-63 (center)
G2-63 (rims)
Cpx-trachydacite
G3-157 (center)
G3-157 (rim)

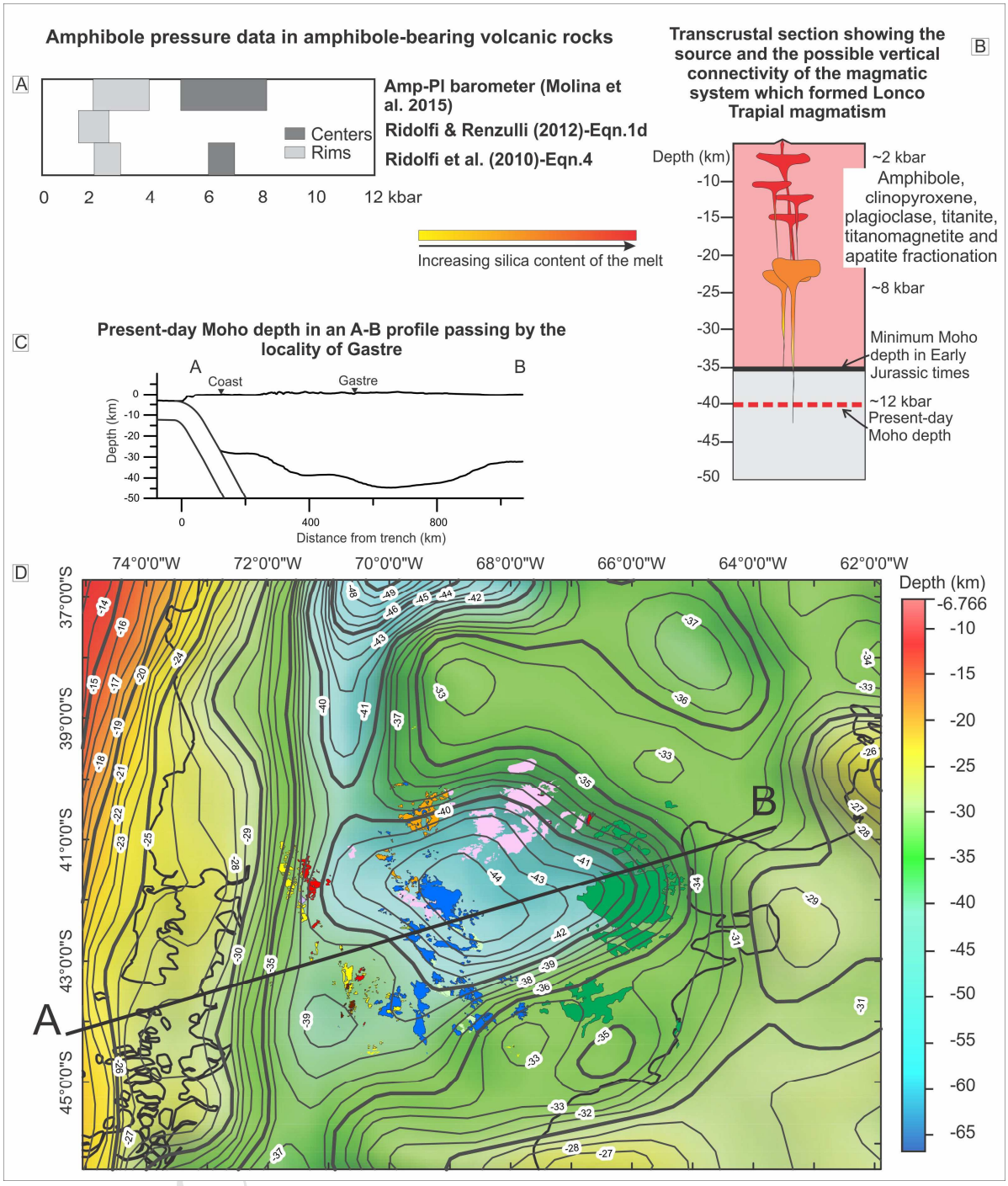
Amphibole pressure data in amphibole-bearing volcanic rocks
A
Centers
Rims
0 2 4 6 8 10 12 kbar
Amp-Pl barometer (Molina et al. 2015)
Ridolfi & Renzulli (2012)-Eqn.1d
Ridolfi et al. (2010)-Eqn.4
Increasing silica content of the melt
Transcrustal section showing the source and the possible vertical connectivity of the magmatic system which formed Lonco Trapial magmatism
B
Depth (km)
-10
-15
-20
-25
-30
-35
-40
-45
-50
~2 kbar
Amphibole, clinopyroxene, plagioclase, titanite, titanomagnetite and apatite fractionation
~8 kbar
Minimum Moho depth in Early Jurassic times
~12 kbar
Present-day Moho depth
C
Present-day Moho depth in an A-B profile passing by the locality of Gastre
A
B
Coast
Gastre
Depth (km)
0
-10
-20
-30
-40
-50
0
400
800
Distance from trench (km)
D
74°0'0"W
72°0'0"W
70°0'0"W
68°0'0"W
66°0'0"W
64°0'0"W
62°0'0"W
37°0'0"S
39°0'0"S
41°0'0"S
43°0'0"S
45°0'0"S
A
B
Depth (km)
-6.766
-10
-15
-20
-25
-30
-35
-40
-45
-50
-55
-60
-65

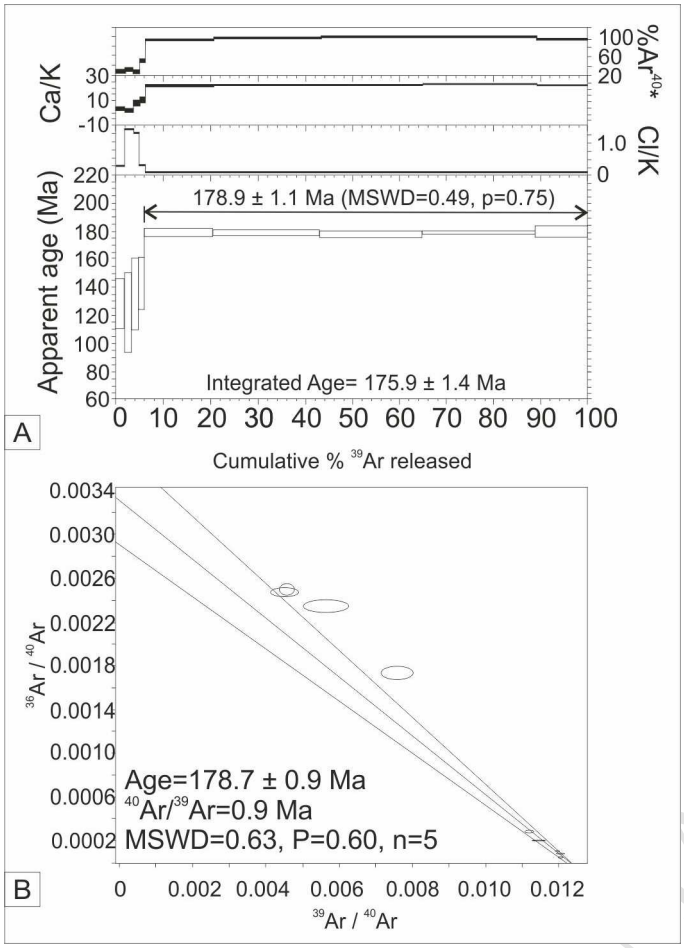

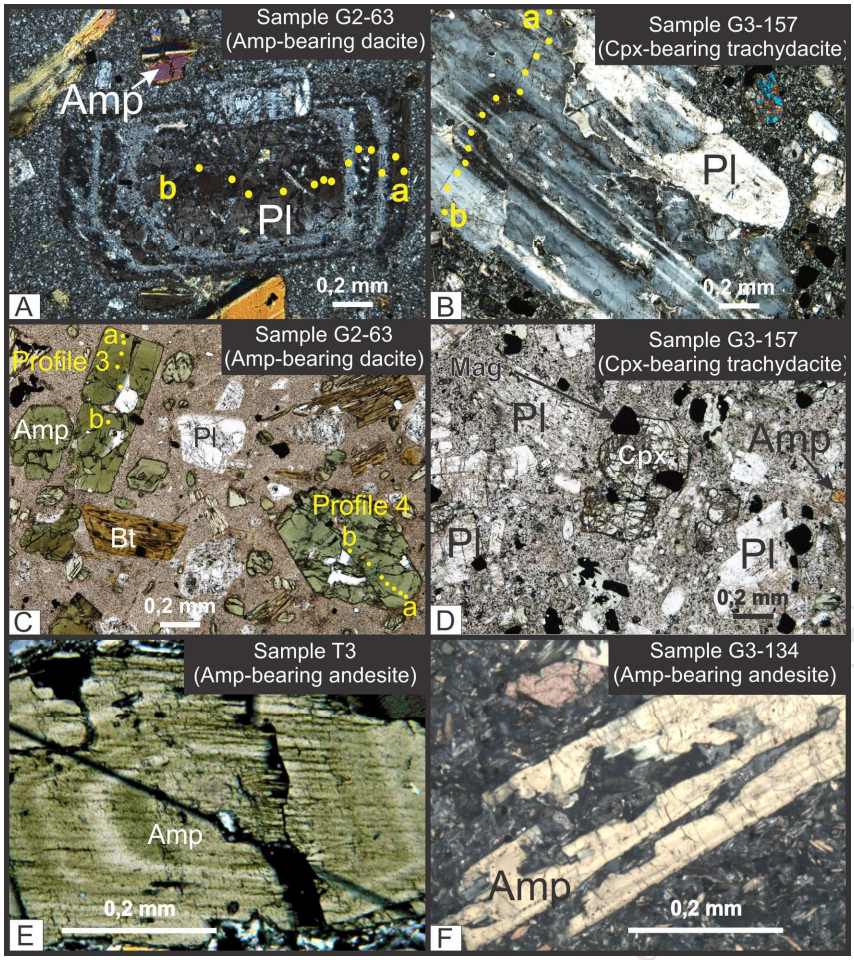

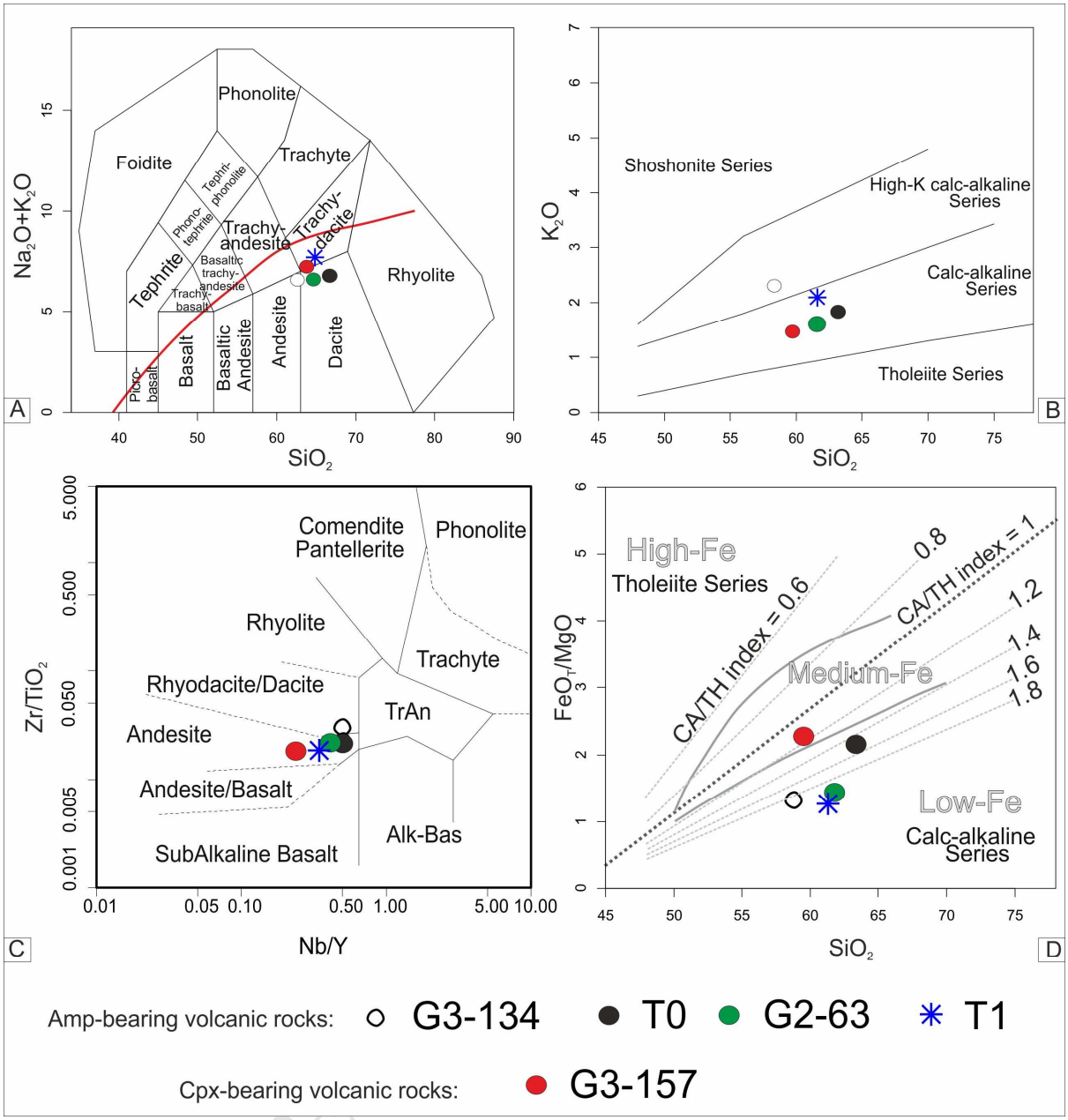
A
Phonolite
Foidite
Trachyte
Tephri-phonolite
Phono-tephrite
Trachy-andesite
Trachy-dacite
Basaltic trachy-andesite
Trachy-basalt
Tephrite
Rhyolite
Phono-basalt
Basalt
Basaltic Andesite
Andesite
Dacite
Na2O+K2O
SiO2
B
Shoshonite Series
High-K calc-alkaline Series
Calc-alkaline Series
Tholeiite Series
K2O
SiO2
C
Comendite Pantellerite
Phonolite
Rhyolite
Trachyte
Rhyodacite/Dacite
TrAn
Andesite
Andesite/Basalt
Alk-Bas
SubAlkaline Basalt
Zr/TiO2
Nb/Y
D
High-Fe
Tholeiite Series
CA/TH index = 0.6
0.8
CA/TH index = 1
1.2
1.4
1.6
1.8
Medium-Fe
Low-Fe
Calc-alkaline Series
FeOT/MgO
SiO2
Amp-bearing volcanic rocks:
G3-134
T0
G2-63
T1
Cpx-bearing volcanic rocks:
G3-157

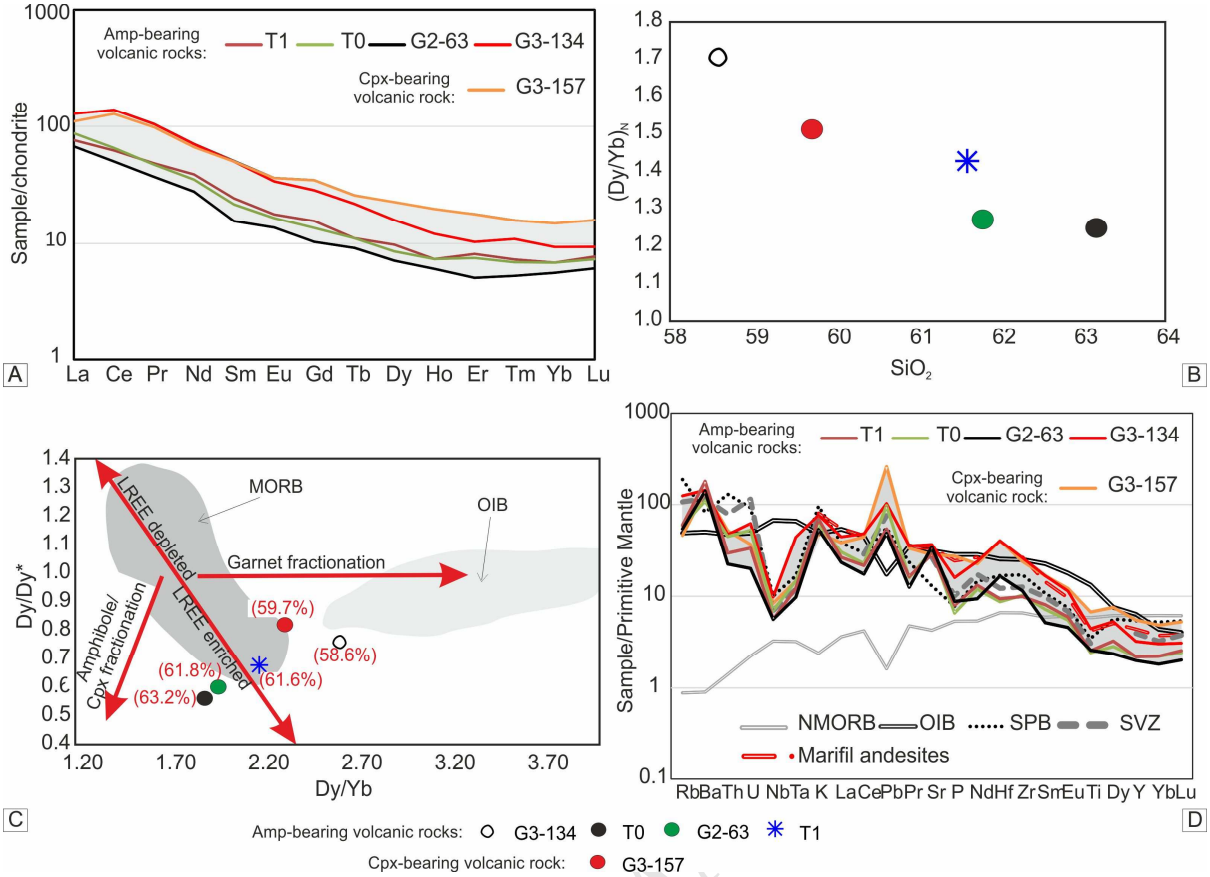

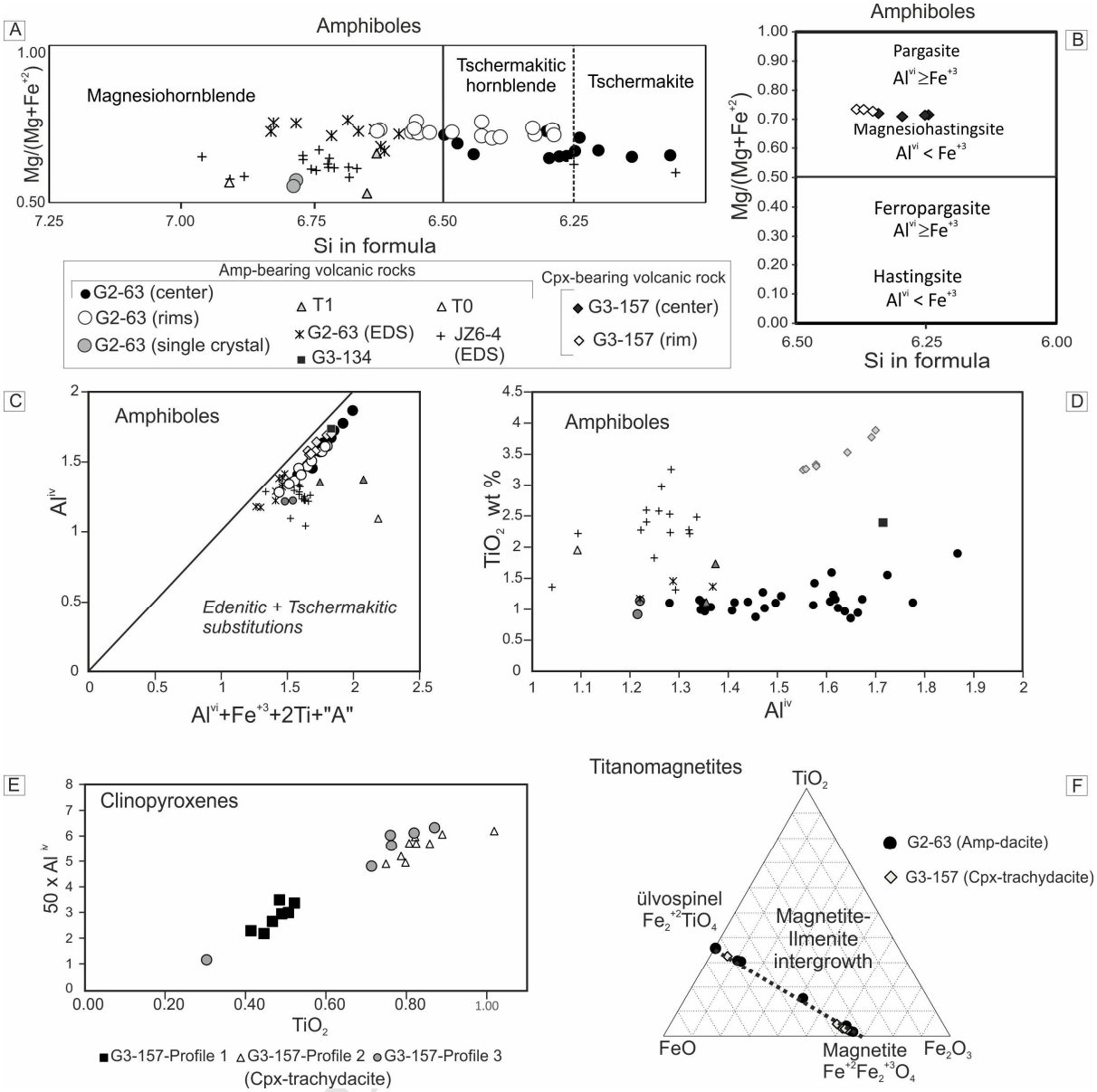
A
Amphiboles
Magnesiohornblende
Tschermakitic hornblende
Tschermakite
Mg/(Mg+Fe+2)
Si in formula
B
Amphiboles
Pargasite
Alvi≥Fe+3
Magnesiohastingsite
Alvi < Fe+3
Ferropargasite
Alvi≥Fe+3
Hastingsite
Alvi < Fe+3
Mg/(Mg+Fe+2)
Si in formula
Amp-bearing volcanic rocks
G2-63 (center)
G2-63 (rims)
G2-63 (single crystal)
T1
T0
G2-63 (EDS)
JZ6-4 (EDS)
G3-134
Cpx-bearing volcanic rock
G3-157 (center)
G3-157 (rim)
C
Amphiboles
Aliv
Edenitic + Tschermakitic substitutions
Alvi+Fe+3+2Ti+"A"
D
Amphiboles
TiO2 wt %
Aliv
E
Clinopyroxenes
50 x Aliv
TiO2
G3-157-Profile 1
G3-157-Profile 2
G3-157-Profile 3
(Cpx-trachydacite)
Titanomagnetites
TiO2
F
G2-63 (Amp-dacite)
G3-157 (Cpx-trachydacite)
ülvospinel
Fe2+2TiO4
Magnetite-
Ilmenite
intergrowth
FeO
Fe2O3
Magnetite
Fe+2Fe2+3O4

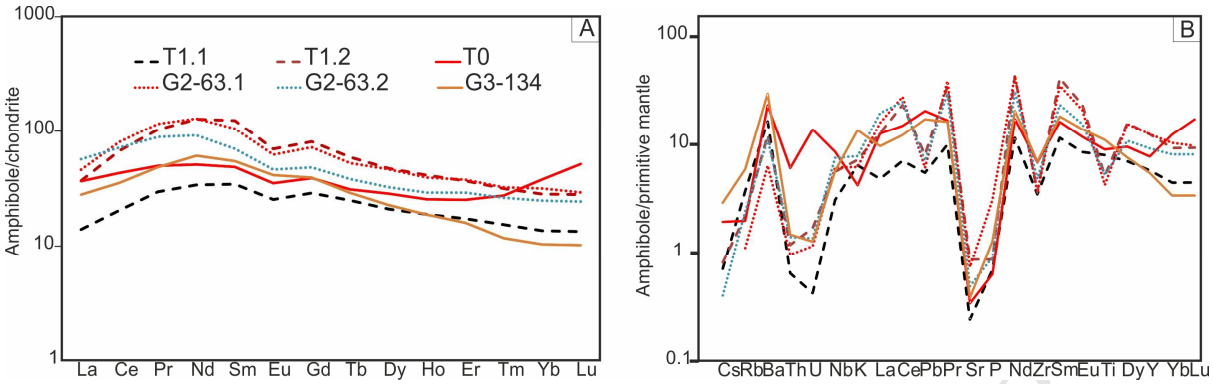

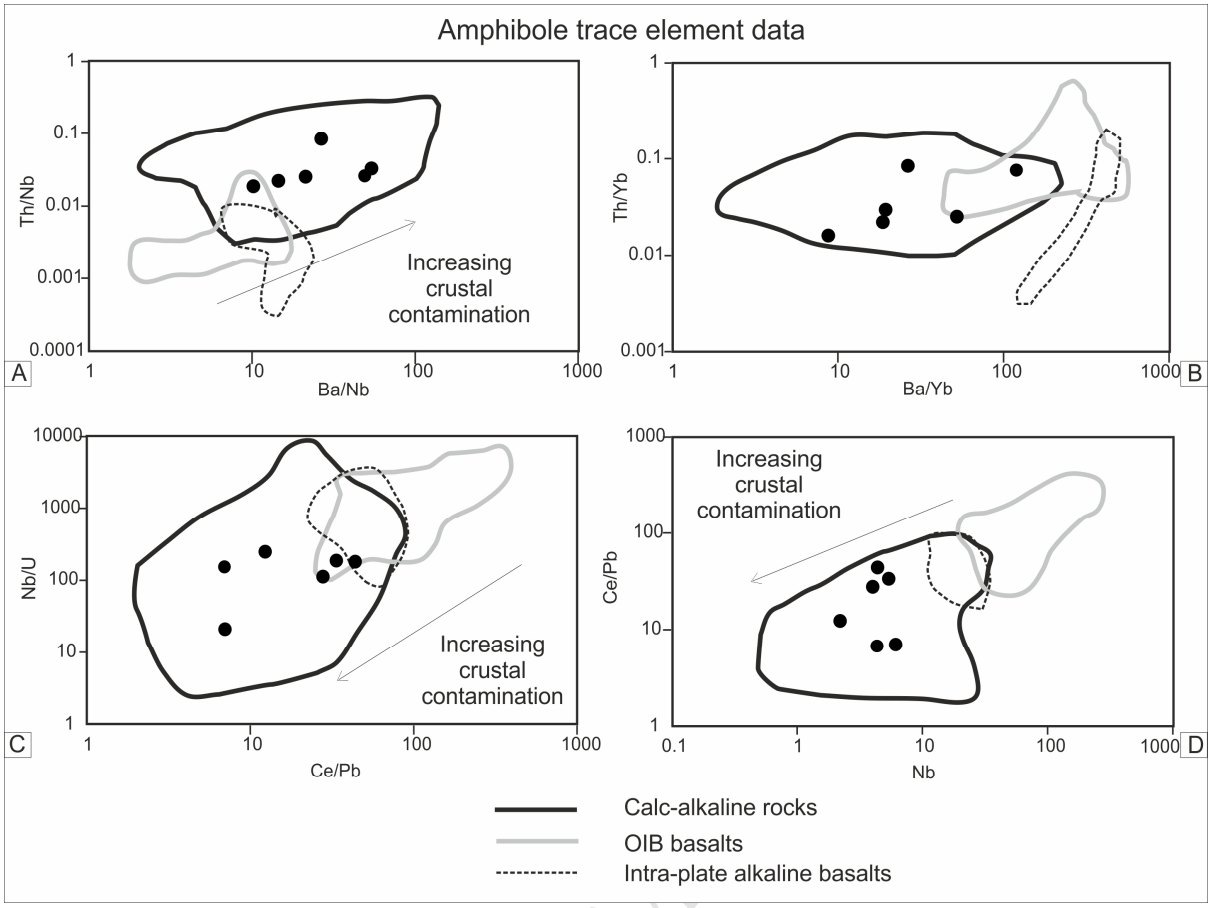

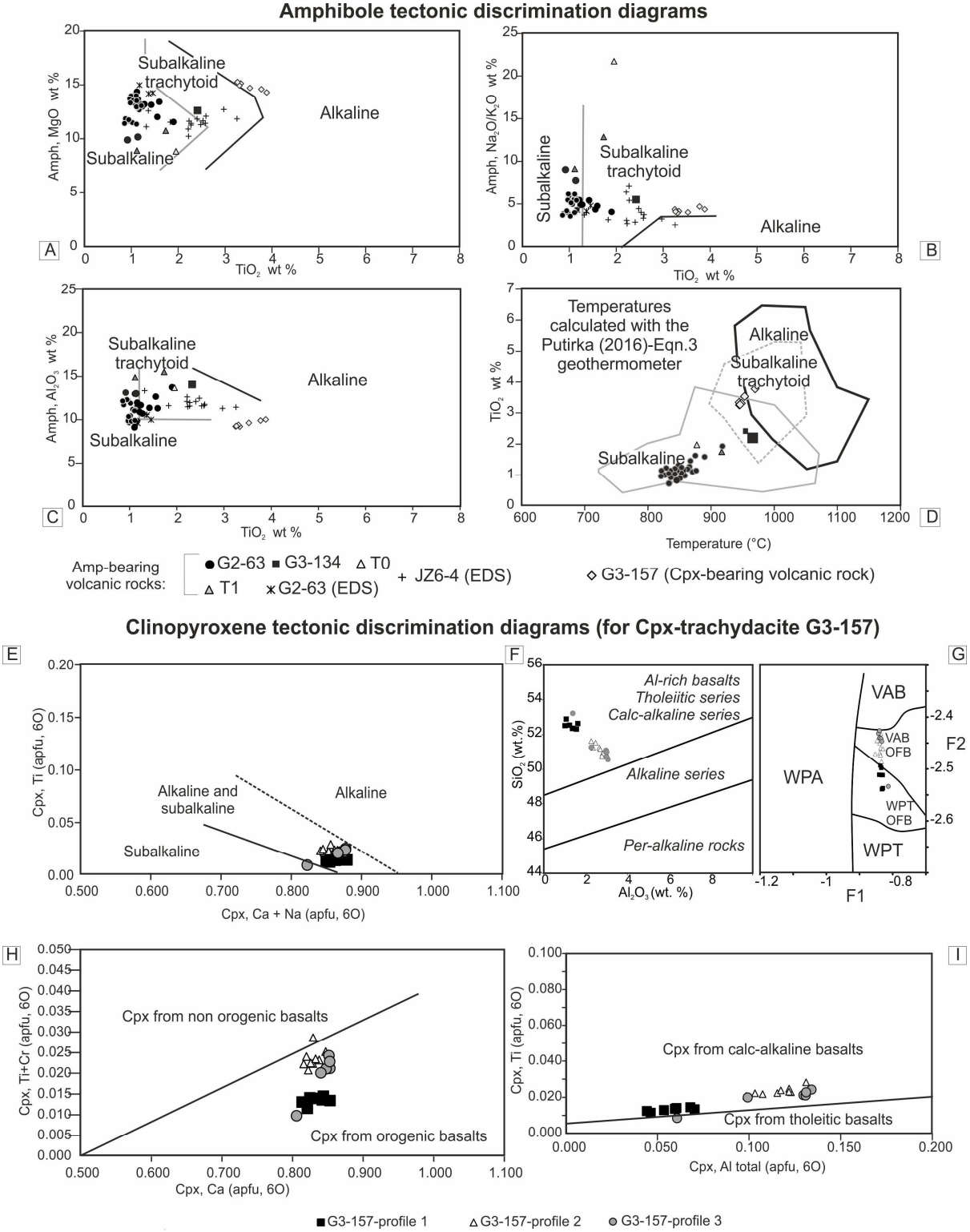
Amphibole tectonic discrimination diagrams
Amph, MgO wt %
TiO2 wt %
Subalkaline trachytoid
Alkaline
Subalkaline
A
Amph, Na2O/K2O wt %
Subalkaline
Subalkaline trachytoid
Alkaline
B
Amph, Al2O3 wt %
Subalkaline trachytoid
Alkaline
Subalkaline
C
TiO2 wt %
Temperatures calculated with the Putirka (2016)-Eqn.3 geothermometer
Alkaline
Subalkaline trachytoid
Subalkaline
D
Temperature (°C)
Amp-bearing volcanic rocks:
G2-63 G3-134 T0
T1 G2-63 (EDS)
+ JZ6-4 (EDS)
G3-157 (Cpx-bearing volcanic rock)
Clinopyroxene tectonic discrimination diagrams (for Cpx-trachydacite G3-157)
E
Cpx, Ti (apfu, 6O)
Alkaline and subalkaline
Alkaline
Subalkaline
Cpx, Ca + Na (apfu, 6O)
F
SiO2 (wt.%)
Al-rich basalts
Tholeiitic series
Calc-alkaline series
Alkaline series
Per-alkaline rocks
Al2O3 (wt. %)
G
VAB
VAB OFB
WPA
WPT OFB
WPT
F2
F1
H
Cpx, Ti+Cr (apfu, 6O)
Cpx from non orogenic basalts
Cpx from orogenic basalts
Cpx, Ca (apfu, 6O)
I
Cpx, Ti (apfu, 6O)
Cpx from calc-alkaline basalts
Cpx from tholeitic basalts
Cpx, Al total (apfu, 6O)
G3-157-profile 1
G3-157-profile 2
G3-157-profile 3

Research highlights

1) A crystallization temperature range between 826 and 916°C was established
2) Shallow to intermediate crystallization depths (2-8 kbar, ~7-26 km) were inferred
3) High oxygen fugacity conditions were found
4) Moho depth in Early Jurassic times did not surpass 35 km
5) Mineral chemistry data was useful to unravel an extensional geochemical signature